Unsteady topography in the eastern Tianshan due to imbalance between denudation and crustal thickening

Julien Charreau, Pierre-Henri Blard, Jérôme Lavé, Stéphane Dominguez, Wang Sheng Li

Tectonophysics 848 (2023) 229702

Unsteady topography in the eastern Tianshan due to imbalance between denudation and crustal thickening

Julien Charreau [a, *], Pierre-Henri Blard [a], Jérôme Lavé [a], Stéphane Dominguez [b], Wang Sheng Li [c]

[a] *CRPG, CNRS, Université de Lorraine, UMR 7358, Vandœuvre-lès-Nancy 54501, France*

[b] *Géosciences Montpellier, Université de Montpellier, UMR CNRS/UMII 5243, Montpellier Cedex 34095, France*

[c] *School of Earth Sciences and Engineering, Nanjing University, 163 Xianlin Ave, Qixia District, Nanjing, Jiangsu Province 210046, China*

Corresponding author: *E-mail addresses:* julien.charreau@univ-lorraine.fr (J. Charreau), pierre-henri.blard@univ-lorraine.fr (P.-H. Blard), jerome.lave@univ-lorraine.fr (J. Lavé), dominguez@umontpellier.fr (S. Dominguez), wangsl@nju.edu.cn (W.S. Li).

Abstract:

The Tianshan mountains have complex and variable topography and documenting their growth is important for understanding both intracontinental mountain building and the evolution of the global climate. We investigate whether this topography is in equilibrium with crustal influx (thickening) and sediment outflux (denudation). Based on literature, we estimate that the eastern Tianshan has been subject to a total crustal shortening rate of ~9.4 mm/a across the Kuitun–Kuche transect, implying ~1.3 mm/a of crustal thickening and a total crustal influx of ~9×10^7 m^3/a. We measured in-situ cosmogenic ^{10}Be concentrations in modern river sands of 34 catchments to constrain recent (0–6 ka) basin-averaged denudation rates within the range and on its two flanks. Denudation rates range from 0.020 ± 0.002 to 0.53 ± 0.07 mm/a, averaging 0.20 ± 0.04 and 0.11 ± 0.02 mm/a in the north and south, respectively; these rates correspond to respective total sediment outfluxes of (542 ± 69) × 10^4 and (164 ± 24) × 10^4 m^3/a. To ensure that these values can be compared to Pleistocene tectonic rates, we reconstructed Pleistocene denudation rates in seven of the studied basins. For this, we determined inherited in- situ cosmogenic ^{10}Be concentrations from 11 cosmogenic depth profiles of abandoned fluvial terraces deposited in the Tianshan piedmonts. These data indicate that denudation rates have been relatively steady since the Pleistocene and thus that recent and Pleistocene sediment fluxes can be compared. These results show that crustal thickening outpaced denudation and sediment outflux by a factor of ~10. Therefore, the Tianshan topography is not in dynamic equilibrium and is growing, even if materials are being subducted into the mantle. Consequently, to sustain this disequilibrium, the range grew laterally. This lateral growth and the inheritance of structures and basins are likely responsible for the complex topography of the range.

https://doi.org/10.1016/j.tecto.2022.229702 Received 29 June 2022; Received in revised form 24 November 2022; Accepted 29 December 2022 Available online 6 January 2023 0040-1951/

1. Introduction

The development of topography strongly influences the evolution of the global climate (Molnar and England, 1990), the construction of mountain belts, mineralization, and species migrations (Antonelli et al., 2009). When, where, how, and how fast topography evolves are fundamental questions with wide implications in Earth sciences (Botsyun et al., 2019). The timing and amplitude of the paleo-topographic development of several large orogens (Andes, Himalaya) have been reconstructed using various approaches including isotopic geochemistry, paleobotany, and palynology, or via the flexural history of the foreland basin (e.g. Curry et al., 2019). Numerical and analogue experiments have also investigated the potential roles of tectonics, climate, and surficial processes during mountain growth (e.g. Avouac and Burov, 1996; Beaumont et al., 1999; Braun, 2006; Whipp et al., 2014), particularly how they may drive the topographic evolution of active orogens (Beaumont et al., 1999; Braun, 2006). These studies mainly predict that the crust behaves as a doubly vergent critical wedge, driven by the crustal strength distribution and the transfer of mass from the eroded uplifting relief to lowland depositional areas (Avouac and Burov, 1996; Braun, 2006). In general, orogenic systems tend toward a thermal, exhumational of steady state (Willett and Brandon, 2002), or a flux and/ or topographic steady state (Burbank, 2002; Willett and Brandon, 2002) in which denudation balances crustal thickening and/or topography does not evolve anymore, respectively (Avouac and Burov, 1996; Dahlen and Suppe, 1988).

However, in Central Asia and particularly the Tianshan, the most active intracontinental region in the world after the Himalaya and an important orographic barrier that also likely played an important role during the onset of Quaternary glaciations by transferring low-salinity fresh water to the Arctic Ocean (Prud'homme et al., 2021), the topography differs significantly from this classical view of orogens with a triangular shape (Fig. 1). Most topography in this region is due to the India-Asia collision, which, since 55 Ma, has rejuvenated pre-existing structures and relief that originally developed during protracted Paleo–Mesozoic collision-subduction processes (Molnar and Tapponnier, 1975), yielding several large, high-elevation, intra-mountain basins sandwiched between intracontinental active mountain belts (Fig. 1). This complex and irregular topography raises broad questions about how topography develops in continental areas. It is unclear if it reflects an immaturity of the orogen and whether a steady state has been reached or not. The role of inherited structures and the distribution of the deformation may also trigger the creation of irregular topography. To investigate how the topography of this range grows we focus here on its state of equilibrium. To this aim one may estimate local surface uplift rates and how they are balanced by denudation. But, because spatial variation of both denudation and crustal thickening are difficult to constrain this task is almost impossible. Moreover, geomorphic processes that drive denudation are highly non-steady state and a full local topographic steady state is probably never achieved (Willett and Brandon, 2002). However, the average form and topography of an orogen can reach a steady state and the simplest approach to investigate it is to balance the fluxes (crustal vs. denudational) across the orogen (Willett and Brandon, 2002).

For instance, preliminary results from the internal Bayanbulak basin (eastern Tianshan; Fig. 1) suggest that erosion and crustal thickening are strongly imbalanced (Charreau et al., 2017). But, how denudation balances tectonics at the scale of the entire range remains poorly known, mainly

because denudation rates spanning the range are underconstrained. Low-temperature thermochronometers mainly record the Paleozoic exhumation history and cannot constrain recent denudation associated with Cenozoic reactivation (e.g. Jolivet et al., 2010). Cenozoic denudation rates have thus been reconstructed from sediment masses stored in the basins surrounding the Tianshan. Métivier and Gaudemer (1997) extrapolated 1D drill core data to 3D sediment volumes in the Junggar and Tarim basins, which bound the Tianshan.

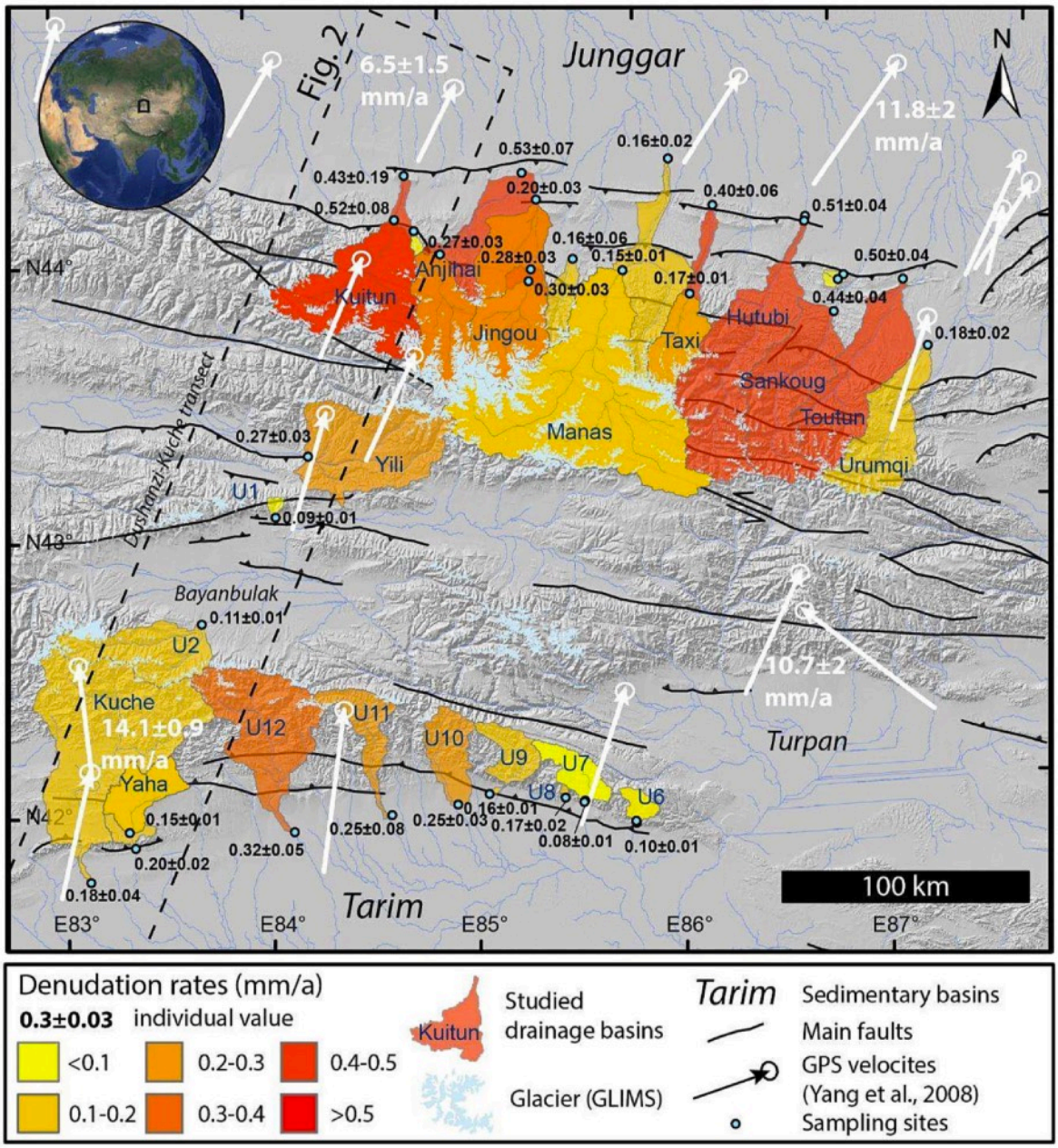

Fig. 1. Hillshaded DEM of the eastern Tianshan, with main faults shown in black. Blue dots indicate modern river sand sampling sites downstream of their corresponding drainage areas, and mean ^{10}Be-derived denudation rates are reported per site. Glaciers are mapped according to the Global Land Ice Measurements from Space (GLIMS) database (Raup et al., 2007). Studied drainage basins are colored according to the mean basin-scale ^{10}Be-derived denudation rates. The dashed box indicates the area shown in Fig. 2b, within which shortening rates have been summed. White arrows are proportional to horizontal GPS velocities

(values re- ported in white text; (Yang et al., 2008)). (For interpretation of the references to colour in this figure legend, the reader is referred to the web version of this article.)

However, the timescales of these volumetric reconstructions are too long (10^6–10^7 a) for a suitable comparison with tectonic rates mainly derived from morphotectonic analyses of deformed Quaternary alluvial marker beds. Over shorter time scales, Guerit et al. (2016) reconstructed the sedimentary volumes stored in several Holocene alluvial fans in the northern Tianshan piedmont and derived corresponding sedimentary fluxes and denudation rates. However, their dataset is insufficient for estimating the total sediment fluxes exported to both Tianshan piedmonts. Mean erosion rates of 0.15 mm/a (ranging from 0.018 to 0.3 mm/a) were also calculated from hydrological measurements of sediment load in the northern Tianshan from 1964 to 2001 (Guan et al., 2022). However, these decadal-scale values may not be representative of rates at the geological time scale. Alternatively, denudation rates over longer time scales (10^2–10^4 a) can be estimated from analyses of in-situ cosmogenic nuclide concentrations in river sediments. Charreau et al. (2011) and Puchol et al. (2017) measured in-situ ^{10}Be cosmogenic concentrations in modern and buried foreland sediments and recon- structed a record of denudation over the last 9 Ma on both sides of the eastern Tianshan (Fig. 1). Nonetheless, their results are limited to only three watersheds covering <5% of the range, impeding accurate estimations of total sediment outfluxes.

Similarly, although numerous studies of active tectonics have provided quantitative estimates of tectonic rates across individual structures, the cumulative tectonic shortening across the entire range and over geological time scales remains poorly known. Tectonic short- ening has only been constrained in the western part of the range where Thompson et al. (2002) estimated a value of $11^{+2/-1}$ mm/a by analyzing morphological markers.

Here, we examine the eastern Tianshan because several morpho-tectonic studies have provided data facilitating the accurate estimation of crustal shortening across the range and thus both crustal thickening and crustal influxes since Pleistocene (<1.4 Ma). By measuring in-situ cosmogenic ^{10}Be concentrations in modern river sands, we also document the recent (0-6 ka) basin-averaged denudation rates of 34 catchments within and on both flanks of the range, which we used to derive sediment fluxes. Using inherited cosmogenic concentrations determined from cosmogenic depth-profile analyses of abandoned fluvial terraces, we also reconstructed 11 Pleistocene denudation rates for seven basins to test the steadiness of denudation rates since the Pleistocene. Finally, we compare sediment and crustal fluxes to discuss the topographic equilibrium of the Tianshan range.

2. Crustal shortening, crustal fluxes, and thickening rates across the eastern Tianshan

2.1. Pleistocene shortening rates

We focused our analyses along the ~340 km long Dushanzi–Kuche transect (Figs. 1, 2), where several morphotectonics analyses of deformed alluvial surfaces previously dated using cosmogenic

nuclides and other approaches (^{14}C, optically stimulated luminescence) provide quantitative estimates of deformation rates across individual structures (Charreau et al., 2020; Charreau et al., 2018; Saint-Carlier et al., 2016). Along this transect, it is possible to sum the crustal shortening recorded across the individual structures to assess the full extent of crustal shortening accommodated across the range. In the northern Tianshan piedmont, deformation along this transect is mainly accommodated across the Dushanzi anticline. Based on detailed fold modeling, cosmogenic and infrared stimulated luminescence ages, and high resolution topographic measurements, we previously estimated the shortening rate across this fold to be 4.3 ± 1 mm/a (Charreau et al., 2018). Based on the excess area method, Su et al. (2018) proposed much lower values of 2.0 ± 1 mm/a, respectively.

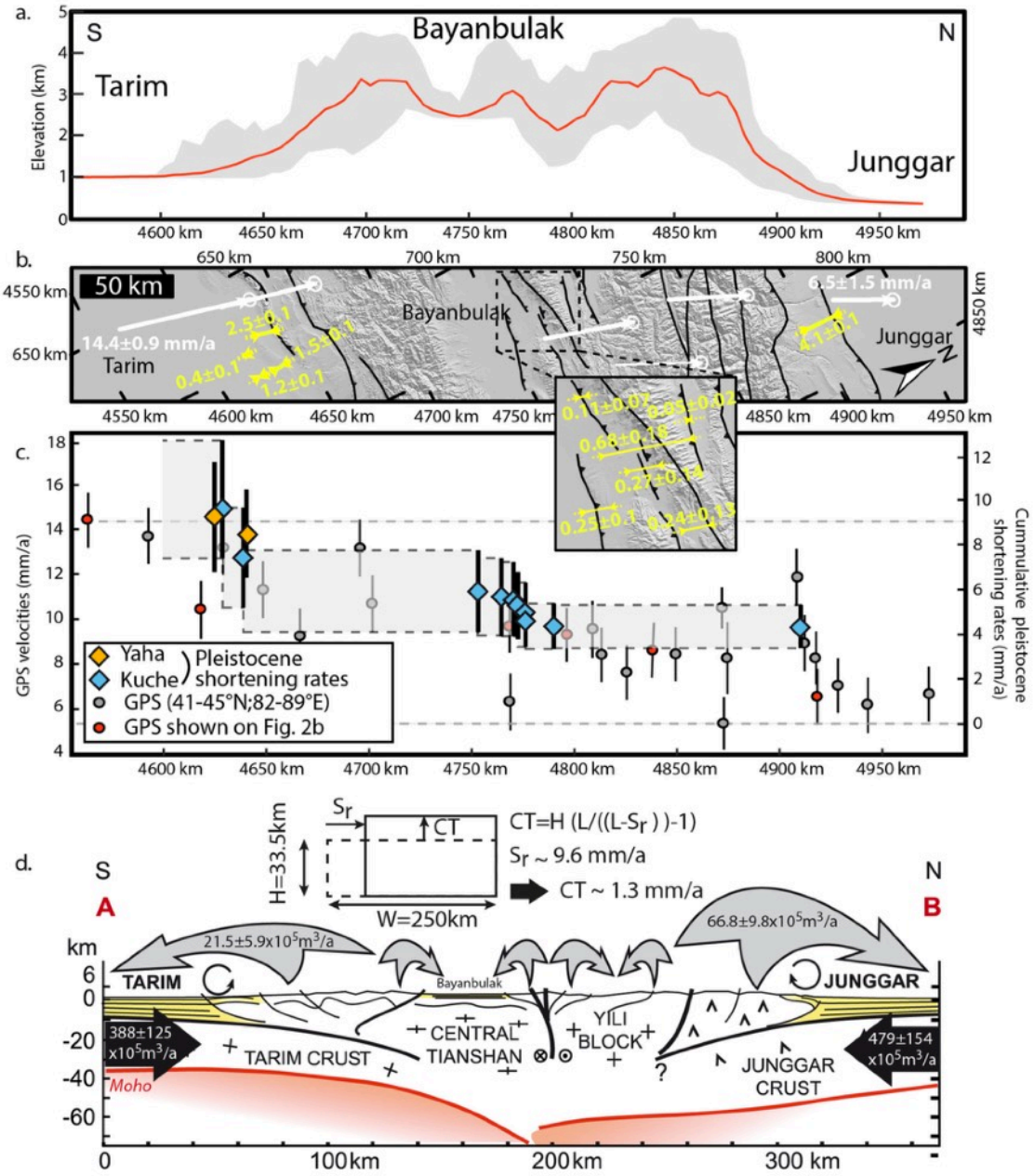

Fig. 2. (a) Swath topographic profile of the Dushanzi-Kuche transect (see Fig. 1). (b) Hillshaded DEM of the transect with horizontal GPS velocities shown in white and Pleistocene tectonic shortening rates in yellow

(see Section 2.1 and Table 2 for data references). The dashed box indicates the area of the outset zoom of the northern side of the Bayanbulak basin. (c) Horizontal GPS velocities (gray and red dots) and cumulative Pleistocene shortening rates (blue diamonds) across the transect. (d) Geological cross section across the range, with crustal and denudation fluxes determined herein. The distances given along axes of Fig. a,b and c correspond to UTM coordinates. The scheme in Fig. 2c illustrates how the crustal thickening rate (CT) was estimated assuming conservation of mass and using a simple shear model based on the thickness of the crust (H) the width of the range (W) and the shortening rate (S_r). (For interpretation of the references to colour in this figure legend, the reader is referred to the web version of this article.)

However, this study likely underestimated the amount of deformation because they neglected the possible diachronicity of the morphological surfaces and sediment aggradation on the back limb of the fold (Charreau et al., 2018). In the interior of the Tianshan range, we previously constrained Pleistocene deformation rates across several individual structures in the Bayanbulak and Nalati basins (Figs. 1, 2) and found the total deformation recorded across the structures of both basins to be 1.6 ± 0.7 mm/a (Charreau et al., 2017) (this value includes a lateral fault not considered in the total value of ~1.4 mm/a given by the authors in their paper). In the southern Tianshan piedmont, deformation is mainly accommodated across the Kuche and Yakeng anticlines. Total Pleistocene deformation rates across these two structures range from 3.3 ± 0.6 to 3.6 ± 1.2 mm/a in the Kuche and Yaha sections, respectively (Charreau et al., 2020). Based on these results, Fig. 2 shows the cumulative Pleistocene shortening accommodated across the Dushanzi–Kuche transect. A total of 9.2 ± 2.4 or 9.6 ± 3.1 mm/a is accommodated across the Dushanzi–Kuche transect during the Pleistocene depending on whether the Kuche or Yaha section is considered, respectively.

2.2. Pleistocene crustal thickening rates and fluxes

Geophysical analyses across the range have constrained the depth of the Moho beneath the Junggar and Tarim basins to be ~35 and ~ 42 km, respectively (Avouac et al., 1993) (Fig. 2). The eroding landscape in the foothills of the two Tianshan piedmonts has likely reached a dynamic equilibrium in which tectonic uplift is balanced by denudation (e.g. Hurtrez et al., 1999), and the denuded material is recycled within the piedmont. Therefore, sediment cover in the Tarim and Junggar basins that is involved in the frontal piedmont structures should be excluded from our mass balance calculation. The deepest decollement observed in the piedmonts' lies at ~5 km depth (e.g. Hubert-Ferrari et al., 2007). Excluding this shallower sedimentary cover thickness, 30 and 37 km of crust are accreted to the Tianshan. Considering the mean value of 33.5 km, assuming pure shear, 9.6 ± 3.1 mm/a of shortening across the ~250-km-long Dushanzi–Kuche transect (i.e. excluding piedmont structures) yields crustal thickening rates of 1.3 ± 0.2 mm/a (Fig. 2). Considering the piedmonts of the eastern Tianshan to be ~270 km along-strike-length (from the Kuitun to the Urumqi basin), assuming steady shortening along strike (see later for a discussion of this assumption) equally distributed on both side of the range (4.8 mm/a), a thickness of the crust of 30 km (35 km–5 km of sediment cover) and 37 km (42 km–5 km of sediment cover) we obtain a crustal influx of 3.9 ± 1.2 × 10^7 m^3/a and 4.8 ± 1.5 × 10^7 m^3/a for the northern and southern piedmonts, respectively. The total crustal influx across the eastern Tianshan range is therefore 8.7 ± 2.7 × 10^7 m^3/a.

3. Recent cosmogenic denudation rates and sediment fluxes

To constrain recent denudation rates across the eastern Tianshan, we collected 34 samples of modern river sands across the range for in-situ cosmogenic ^{10}Be analyses (Fig. 1; Tables 1, 2). This includes data from the internal part of the range previously analyzed by Charreau et al. (2017). We focused on the main tributaries to document denudation rates across most of the entire range. River sands were mainly sampled at the outlets of the high range, but some samples were collected downstream of the piedmonts to investigate sediment recycling and storage. All samples were treated (quartz enrichment, ^{10}Be extraction) in the cosmogenic laboratory at the Centre de Recherches Pétrographiques et Géochimiques (CRPG). All samples were sieved to isolate the 200–800 μm fraction. The quartz fraction was first enriched through successive magnetic separations. To eliminate all other remaining mineral phases, the quartz-enriched fraction was successively leached in a mixture of 4/5 H_2SiF_6 + 1/5 HCl. The isolated quartz fraction then underwent three partial dissolutions in concentrated HF, removing 30% of the quartz, to eliminate atmospheric ^{10}Be (Brown et al., 1991). The purified quartz fraction was then spiked with 100 μL of a carrier solution containing 3025 ppm ^{9}Be before being completely dissolved in HF. Following subsequent purification in chromatographic columns by anion exchange, cation exchange, alkaline precipitations, and oxidation, the purified beryllium and aluminum oxides were analyzed at the French national accelerator mass spectrometer facility ASTER (Accelerator for Earth Sciences, Environment and Risks, CEREGE Laboratory, Aix en Provence, France). ^{10}Be/^{9}Be ratios measured at ASTER were normalized using the NIST SRM 4325 reference material (^{10}Be/^{9}Be = (2.79 ± 0.03) × 10^{-11}). This standardization is equivalent to 07KNSTD within rounding errors (Nishiizumi et al., 2007). Total analytical ^{10}Be/^{9}Be blank ratios were, on average, (1.5 ± 0.8) × 10^{-15} (see Supplementary Table A). The complete raw cosmogenic ^{10}Be data are reported in Supplementary Table A and summarized in Table 1. In-situ cosmogenic ^{10}Be concentrations ranged from (2.99 ± 0.20) × 10^{4} to (30.3 ± 1.4) × 10^{4} at/g. Denudation rates were calculated using these concentrations and basin-averaged production rates using the GIS tool Basinga, which approximates muogenic production rates at depth using exponential laws (Charreau et al., 2019) (Table 1). Latitude- and elevation-scaling was performed using the Stone model (Stone, 2000), a 90-m-resolution S.R. T.M (Shuttle Radar Topographic Mission) D.E.M (Digital Elevation Model), the ERA-40 atmosphere atlas (Uppala et al., 2005), and the average S.L.H.L (Sea Level High Latitude) ^{10}Be production rate computed from the global production rate dataset in CREp (Martin et al. (2017), and references therein). We also calculated topographic corrections using the GIS tool of Codilean (2006). Quartz-free areas were mapped by digitizing thirty-two 1:200,000-scale Chinese geological maps (Bureau of the Geological and the Mineral Resources of the Xinjiang Uygur Autonomous Region (1985) and were excluded from the calculation. Nevertheless, these geological maps group different lithologies, implying potential uncertainties on the presence of quartz in the watersheds. Hence, the presence or absence of quartz can only be established with certainty in a limited number of cases. That said, this quartz correction affected the calculated ^{10}Be production rate by <5%.

Table 1
Summary of in-situ ^{10}Be cosmogenic concentrations measured in present-day river sediments around the Tianshan and corresponding basin-averaged cosmogenic production rates and denudation rates. Uncertainties are given with 1σ. Means are weighted averages. Neutron, Slow muons and Fast muons are the cosmogenic production rates for spallation (neutron), slow and fast muon capture. *indicate sample that were excluded for flux and averaging calculation because they were collected downstream in the piedmont and were likely biased by sediment reworking (see discussion for more details).

Sampling						Production rates						Denudation rates	Time scale	Basin Area	Sediment fluxes
Sample	River	Date	Lat.	Long.	^{10}Be	Topo factor	Glacial cover	Neutron	Slow muons	Fast muons	Total				
			(°)	(°)	(10^4 at/g)		%	(at/g/a)				(mm/a)	ka	10^3 km^2	10^5 m^3/a
Northern Tianshan (main rivers)															
KTNRB	Kuitun	2009	44.2933	84.7905	4.8 ± 2.1	0.99	8.0	33.00	0.03	0.05	33.08	0.43 ± 0.19	1.4	1.93	9.4 ± 2.7
KTNDam	Kuitun	2009	44.1342	84.7311	4.1 ± 0.6	0.99	14.8	33.01	0.03	0.05	33.09	0.52 ± 0.08	1.2	2.03	
TS10–21	AnjiHai	2010	44.2835	85.3900	3.4 ± 0.4	0.99	14.6	27.90	0.03	0.05	27.97	0.53 ± 0.07	1.1	1.76	*
TS09_ANJI	AnjiHai	2009	44.0023	84.9556	5.2 ± 0.6	0.99	20.7	33.15	0.03	0.05	33.23	0.27 ± 0.03	2.2	1.05	2.9 ± 0.3
TS09_JIN2	Jingou	2009	43.9300	85.4105	6.8 ± 0.5	0.99	19.5	31.75	0.03	0.05	31.83	0.3 ± 0.03	2.0	1.16	3.4 ± 0.4
TS10–20	Jingou	2010	44.1831	85.4556	8.9 ± 1.2	0.99	14.3	28.85	0.03	0.05	28.92	0.2 ± 0.03	2.9	1.88	
TS09_JIN1	Jingou	2009	43.8879	85.3968	7.6 ± 0.6	0.99	21.5	32.68	0.03	0.05	32.76	0.28 ± 0.03	2.2	1.06	
TS10–22	Ningjia	2010	43.9598	85.6252	13.2 ± 5	0.99	6.5	32.40	0.03	0.06	32.48	0.16 ± 0.06	3.8	0.30	0.5 ± 0.2
TS10–23	Manas	2010	43.9093	85.8728	14.9 ± 0.5	0.99	14.7	37.61	0.03	0.06	37.69	0.16 ± 0.01	3.8	4.47	7.8 ± 0.7
TS10–24	Manas	2010	44.3043	86.1375	14.3 ± 1.3	0.99	12.8	34.07	0.03	0.05	34.15	0.15 ± 0.02	3.9	5.57	
TS12-TXH-RB	Taxi	2012	44.1258	86.3472	4.6 ± 0.7	0.99	8.6	29.62	0.03	0.05	29.70	0.4 ± 0.06	1.5	0.76	*
TS09_TA2	Taxi	2009	43.8089	86.2044	12.6 ± 0.5	0.99	10.5	33.60	0.03	0.06	33.69	0.17 ± 0.01	3.6	0.59	1 ± 0.1
Uru	Urumqi	2012	43.5627	87.3803	11.9 ± 0.8	0.99	4.0	33.11	0.03	0.06	33.19	0.18 ± 0.02	3.4	1.23	2.2 ± 0.2
TS10–25	Hutubi	2010	44.0620	86.8129	3.9 ± 0.2	0.99	4.1	31.56	0.03	0.06	31.65	0.51 ± 0.04	1.2	2.23	11.4 ± 0.9
TS10–26	Sankoung	2010	43.7111	86.9237	4.2 ± 0.3	0.99	2.9	29.48	0.03	0.06	29.57	0.44 ± 0.04	1.4	1.71	7.6 ± 0.7
TS10–27	Toutun	2010	43.8088	87.2808	3 ± 0.2	0.99	1.6	23.11	0.02	0.05	23.19	0.5 ± 0.05	1.2	1.61	8.1 ± 0.7
												0.2 ± 0.04	3.0		54.2 ± 6.9
(Secondary tributaries)															
TS09_KUI1	U1	2009	44.0900	84.8283	20.6 ± 5.2	1.00	0.0	26.75	0.03	0.06	26.84	0.08 ± 0.02	7.3	0.03	0.03 ± 0.01
TS09_MA1	U2	2009	43.8413	86.9854	30.3 ± 1.4	1.00	0.0	11.09	0.02	0.05	11.15	0.02 ± 0.002	24.9	0.02	0.01 ± 0
TS09_MA2	U3	2009	43.8252	86.9551	12.9 ± 0.4	1.00	0.0	11.69	0.02	0.05	11.75	0.06 ± 0.004	10.1	0.03	0.02 ± 0
Central Tianshan															
TS12-BBKS-RB	U4	2012	42.6895	83.6916	22.7 ± 1.8	0.99	9.6	40.12	0.03	0.06	40.21	0.11 ± 0.01	5.4	1.03	1.1 ± 0.1
TS12-Yili-RB	Zeketai	2012	43.2884	84.2485	7.3 ± 0.8	1.00	3.0	31.76	0.03	0.06	31.85	0.27 ± 0.03	2.3	1.82	1.82
TS12-BBK-RB	U5	2012	43.0698	84.0753	28 ± 1.5	1.00	0.0	38.99	0.03	0.06	39.08	0.09 ± 0.01	6.7	0.04	0.04 ± 0
												0.1 ± 0.01	6.0		
Southern Tianshan															
TS10–01	U6	2010	41.9006	85.7879	16 ± 0.8	0.99	0.0	30.81	0.03	0.06	30.90	0.09 ± 0.01	6.3	0.14	0.13 ± 0.01
TS10–03	U6	2010	41.9072	85.7860	14.5 ± 1.3	0.99	0.0	30.84	0.03	0.06	30.93	0.1 ± 0.01	5.8	0.14	0.14 ± 0.02
TS10–04	U7	2010	42.0059	85.4460	7.3 ± 0.6	0.99	0.0	19.34	0.02	0.05	19.41	0.17 ± 0.02	3.5	0.02	0.03 ± 0
TS10–05	U8	2010	42.0330	85.0758	12.3 ± 0.8	0.99	0.0	32.04	0.03	0.06	32.13	0.16 ± 0.01	3.9	0.39	0.6 ± 0.05
TS10–06	U9	2010	41.9991	84.9186	6.8 ± 0.8	0.99	0.0	27.39	0.03	0.06	27.48	0.25 ± 0.03	2.4	0.56	1.42 ± 0.19
TS10–07	U10	2010	41.9714	84.5950	8 ± 2.4	0.99	1.6	32.42	0.03	0.06	32.51	0.25 ± 0.08	2.4	0.53	1.34 ± 0.41
TS10–08	U11	2010	41.9234	84.1138	6.5 ± 0.9	0.99	3.0	31.61	0.03	0.06	31.70	0.32 ± 0.05	1.9	1.68	5.32 ± 0.79
TS10–09	Yaha	2010	41.8813	83.3340	6.1 ± 0.4	1.00	0.0	19.46	0.02	0.05	19.54	0.2 ± 0.02	3.0	0.66	1.1 ± 0.1
TS10–10	Yaha	2010	41.9397	83.3068	8.2 ± 0.3	1.00	0.0	19.55	0.02	0.05	19.63	0.15 ± 0.01	3.9	0.55	
TS10–11	Kuche	2010	41.7606	83.1128	10.3 ± 2.1	0.99	1.4	33.52	0.03	0.06	33.61	0.18 ± 0.04	3.3	3.19	5.7 ± 1.3
TS10–13	U13	2010	41.9919	85.5417	24.1 ± 1.1	0.99	0.0	32.24	0.03	0.06	32.34	0.08 ± 0.01	7.2	0.37	0.3 ± 0
TS10–14	U13	2010	41.9867	85.5381	22.9 ± 1	0.99	0.0	32.24	0.03	0.06	32.34	0.09 ± 0.01	6.9	0.37	0.3 ± 0
												0.11 ± 0.02	5.5		16.4 ± 2.9

Table 2
Late Pleistocene denudation rates derived from cosmogenic depth profiles reported in the literature. ε and ε_n are absolute late Pleistocene rates and those normalized to recent denudation rates, respectively. The superscript 'g' indicates rates calculated including glacial cover within the drainage basin (see Section 4.1).

Basin	Profile name	Coordinates		Terrace age	Inherited concentration	ε^g	ε_n^g	ε	ε_n	References
		Lat. (°)	Lon.(°)	(ka)	(10^3 at/g)	(mm/a)		(mm/a)		
Kuitun	KTN-T3	44.3005	84.7763	13 ± 2	64.4 ± 13.1	0.37 ± 0.08	0.7 ± 0.2	0.4 ± 0.08	0.8 ± 0.2	Charreau et al. (2018)
Kuitun	KTN-T0	44.2901	84.7599	116 ± 15	40.9 ± 2.8	0.58 ± 0.05	1.1 ± 0.2	0.62 ± 0.06	1.2 ± 0.1	Puchol et al. (2017)
Anjihai	ANJ-T1B	44.1052	85.0973	5.1 ± 1.7	99.6 ± 9	0.25 ± 0.03	0.9 ± 0.1	0.29 ± 0.03	1.1 ± 0.1	Malatesta and Avouac (2018)
Jingou	JGH-T0	44.1731	85.4584	66 ± 5	100 ± 3	0.24 ± 0.02	0.9 ± 0.1	0.29 ± 0.02	1.1 ± 0.1	Puchol et al. (2017)
Yaha	YAK1	41.8001	83.3193	130 ± 9	63 ± 9	0.19 ± 0.03	1 ± 0.2	0.19 ± 0.03	1 ± 0.2	Saint-Carlier et al. (2016)
Yaha	Ya-T1	41.8818	83.3289	68.3 ± 10.3	88.6 ± 14.4	0.13 ± 0.02	0.7 ± 0.1	0.13 ± 0.02	0.7 ± 0.1	Charreau et al. (2020)
Kuche	KU1	41.7609	83.1057	140 ± 17	49 ± 34	0.37 ± 0.26	2.4 ± 1.7	0.39 ± 0.27	2.5 ± 1.8	Saint-Carlier et al. (2016)
Kuche	KU2	41.7625	83.1145	65 ± 5	94 ± 16	0.19 ± 0.04	1.2 ± 0.3	0.2 ± 0.04	1.3 ± 0.2	Saint-Carlier et al. (2016)
Bayanbulak	BBK4-T2	43.0467	84.1445	64 ± 6	189 ± 50	0.12 ± 0.03	1.4 ± 0.4	0.12 ± 0.03	1.4 ± 0.4	Charreau et al. (2017)
Bayanbulak	BBK3-T2	43.0690	84.0747	22 ± 2	183 ± 14	0.14 ± 0.01	1.5 ± 0.2	0.14 ± 0.01	1.5 ± 0.2	Charreau et al. (2017)
Bayanbulak	BBK3-T3	43.0712	84.0713	91 ± 11	136 ± 136	0.18 ± 0.18	2 ± 2	0.18 ± 0.18	2 ± 2	Charreau et al. (2017)
						Weighted mean:	0.9 ± 0.1		0.8 ± 0.1	

Following Delunel et al. (2010), we also excluded low-slope areas (<3°) from the production rate calculation because they are unlikely to be sediment sources or affected by stream network transport, and represent depositional zones that do not provide sediments to the river. Shielding by snow cover was neglected because it remains difficult to constrain due to the lack of field-based data on snow cover, snow depth, and their seasonal evolution in the Tianshan. Rigorously, neglecting snow shielding implies that denudation rates are overestimated. To account for possible glacial shielding, production rates in glacial areas were assumed to be 0 at/g/a (e.g. Delunel et al., 2010). These areas were determined using the Global Land Ice Measurements from Space (GLIMS) glacier database (Raup et al., 2007) for modern sediments. The glacier corrections amount in average to 9% for modern sediments.

Recent denudation rates range from 0.020 ± 0.002 to 0.53 ± 0.07 mm/a (Table 1). Denudation rates along the main tributaries on both sides of the range are, on average, higher than those in small basins within the piedmont (KUI1, MA1, and MA2) and in the central part of the range. On average, denudation rates are higher in the northern piedmont than in the southern piedmont (means of 0.20 ± 0.04 and 0.11 ± 0.02 mm/a, respectively). In the central part of the range, denudation rates are very low (mean 0.10 ± 0.01 mm/a). We did not observe any change along strike within the range. Table 1 also provides the sediment fluxes calculated based on these recent denudation rates and the cor- responding drainage areas. The total sediment outfluxes in the analyzed watersheds are $(542 \pm 69) \times 10^4$ and $(164 \pm 24) \times 10^4$ m^3/a in the north and south, respectively.

4. Discussion

4.1. Robustness of cosmogenic denudation rates

Our ^{10}Be-derived denudation rates and sediment fluxes are higher than those determined from alluvial fan volumetric reconstructions (Guerit et al., 2016) and sediment gauging (e.g. Guan et al., 2022; Liu et al., 2011). We consider five possible reasons for this discrepancy. First, only loose depositional ages are available for the fans studied by Guerit et al. (2016); hence, their derived fluxes end denudation rates have large uncertainties. Second, sediment bed load fluxes are difficult to measure, and total sediment fluxes measured by gauging could be underestimated. Third, the lowest denudation rate derived from gauging (0.02 mm/a) was measured in the upper part of the Urumqi River (Liu et al., 2011), where the glacial morphology and U-shaped valley have been well preserved. Consequently, the fluvial incision rate is most likely low and the derived denudation rates are not representative of the entire Urumqi basin and Tianshan region. Four, millennium-scale cosmogenic denudation rates are commonly higher than decadal-scale gauging rates because sediment delivery can be episodic and gauging monitoring may not capture larger events more representative of longer term rates (e.g. Ferrier et al., 2005). Fifth, the wind is efficient in the Tianshan and may have eroded and transported sediments far away from the rivers and alluvial fans.

Nevertheless, it is fair to question whether our ^{10}Be-derived denudation rates are overestimated due to the incorporation of ^{10}Be-depleted sedimentary materials. Given the size of the studied drainage basins and the arid regional climate, it is unlikely that the measured in-situ cosmogenic concentrations were biased by the incorporation of coarse deep landslide materials with low cosmogenic concentrations.

Along the Kuitun River (Fig. 1), Jolivet et al. (2014) reported that several thick conglomerate deposits hang on the valley flanks at high elevations. Fill-cut terraces, slope colluvium deposits, and glacial moraines are also present in most of the studied valleys (Jolivet et al., 2014). Below the high range, most rivers drain the foreland piedmont, where they incise thick Neogene to Quaternary sediments that have been uplifted across the foreland fold and thrust belts. Yet, if depleted in cosmogenic nuclides, the recycling of such sediments temporarily stored within valleys or foreland piedmonts could lower the cosmogenic concentrations of river sands and hence artificially increase the basin-averaged denudation rate. To estimate the potential impact of this bias, we calculated the deviation of denudation rates with respect to the proportion of transitory sediments recycled in the river for several eroded thicknesses and storage durations (Figs. 3, 4). We considered alluvial or colluvial sediments with inherited cosmogenic concentrations that depend on the average denudation rate of the drainage basin.

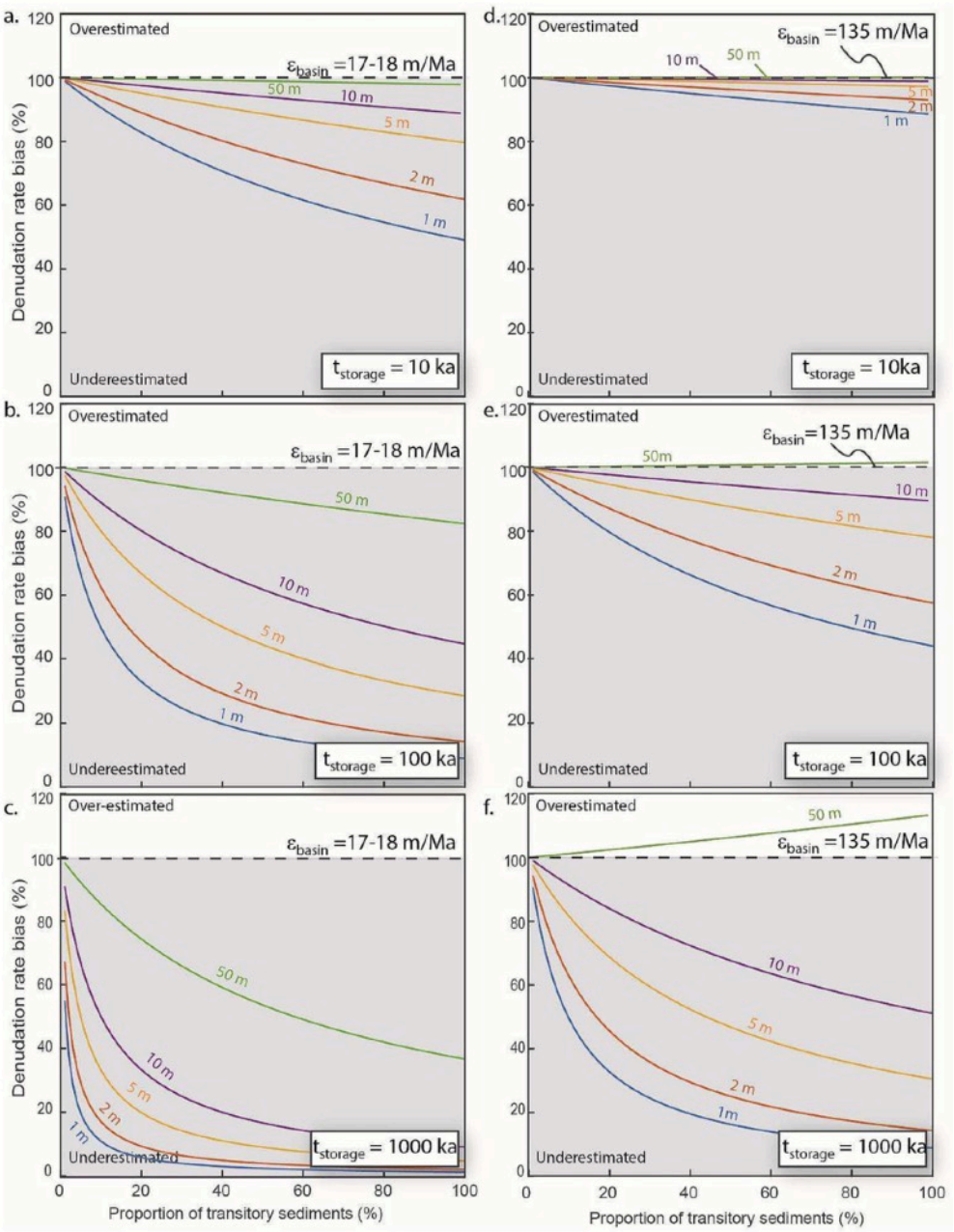

Fig. 3. Denudation rate biases induced by the recycling of transitory alluvial sediments assuming 'true' basin-averaged denudation rates of (a–c) 17–18 m/Ma and (d–f) 135 m/Ma. Biases were estimated for different thicknesses of recycled sediments (1, 2, 5, 10, and 50 m) and three different storage durations (10, 100, and 1000 ka). See Section 4.1 for details.

To calculate the inherited concentrations, we considered previously published lower basin-averaged denudation rates (Guan et al., 2022; Guerit et al., 2016; Jolivet et al., 2014; Liu et al., 2011). We considered two cases: the extreme gauging value of 17–18 m/Ma measured in the Urumqi valley by Liu et al. (2011) and 135 m/Ma which is the average rate derived from alluvial fan reconstruction (Guerit et al., 2016). We assumed an average cosmogenic production rate of ~25 at/g/a (25.25, 0.027, and 0.054 for neutrons and slow and fast muons, respectively) as representative of drainage basins in the Tianshan piedmonts (Table 1). Based on these initial theoretical ^{10}Be concentrations, we estimated the depth evolution of nuclide concentrations if those denuded materials were

temporarily stored in the basin (in terraces or slope deposits) for durations of 10, 100, and 1000 ka and re-exposed to cosmic rays under the same production rates.

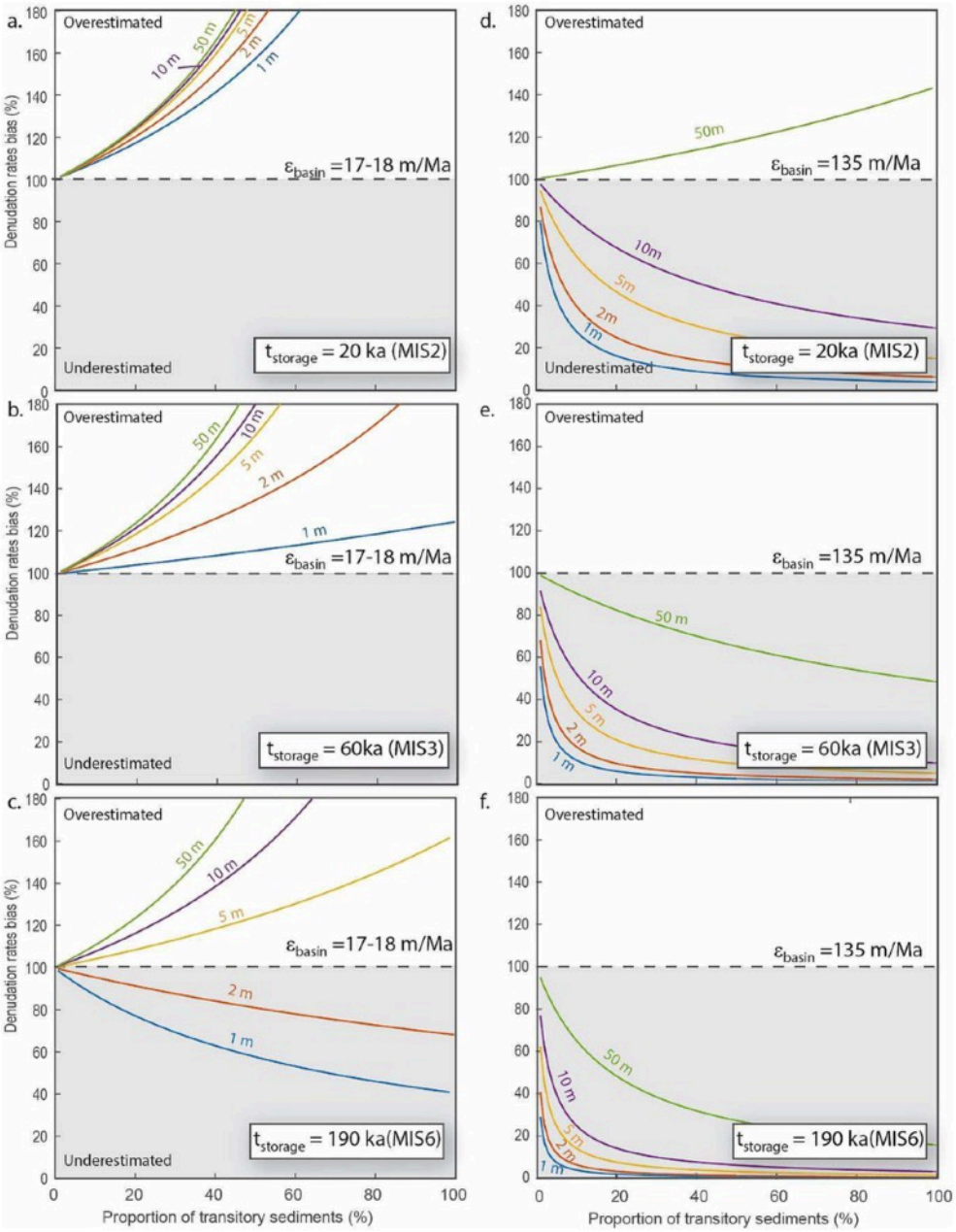

Fig. 4. Denudation rate biases induced by the recycling of transitory glacial sediments assuming 'true' basin-averaged denudation rates of (a–c) 17–18 m/Ma and (d–f) 135 m/Ma. The cosmogenic ^{10}Be concentration of the glacial sediments is assumed null before storage. Biases were estimated for different thicknesses of recycled moraines (1, 2, 5, 10, and 50 m) and three different time of storage durations (20, 60, and 190 ka), which correspond to the main stages of glacial advance recorded in the Tianshan (Li et al., 2014). See Section 4.1 for details.

These theoretical concentrations represent the potential ^{10}Be contributions of sediments previously stored on the basin slopes. Finally, we estimated the ^{10}Be concentrations of river sediments under

different mixing scenarios, from exclusively primary denuded materials to exclusively recycled transitory sediments (Fig. 3).

Our calculation shows that most scenarios involving sediment recycling result in a decrease of the apparent denudation rate, which is at odds with our ^{10}Be-derived denudation rates being higher than those of Guan et al. (2022). In contrast, our model shows that denudation rates are only overestimated when a large proportion (>50%) of old (>1 Ma), thick (>50 m) stored alluvial sediments is recycled within the river (Fig. 3). However, in high-range river valleys upstream of the foreland piedmont, the volume of old transitory alluvial deposits is likely too low to account for such a high proportion of river sediments at the outlet of the high range. Moreover, this bias does not exceed +10–20% (Fig. 3f) and is therefore already encompassed within the uncertainties on the denudation rates themselves. Furthermore, such an overestimation is insufficient to explain our values that are in average 2–10 times greater than previously estimated rates (Guan et al., 2022; Guerit et al., 2016). It is therefore unlikely that our samples that were collected at the outlet of the high range, and thus upstream of foreland sediments, were significantly impacted by the recycling of ^{10}Be-depleted alluvial sediments. Another observation also supports this conclusion: in the Kuitun, Jingou, and Manas Rivers (northern Tianshan), samples collected downstream of the foreland piedmont do not show any particular concentration changes, within uncertainties, from those collected farther upstream at the outlet of the high range (Table 1, Fig. 5). Two exceptions are the Taxi and Anjihai Rivers; the ^{10}Be concentrations in their downstream sediments are 40–50% lower than at the outlet of the high range (Fig. 5), suggesting the recycling of thick, old, ^{10}Be-depleted foreland deposits. The corresponding denudation rates obtained for these two downstream samples should therefore only be considered maxima and are thus dis- regarded from later calculations. In the southern piedmont, the bias is probably also negligible because the incision of the Neogene foreland sediments is lower than in the Northern Tianshan. The proportion of Neogene rocks exposed at the surface and potentially eroded is also lower (see for example geological maps of Charreau et al., 2006; Huang et al., 2006; Sun et al., 2009a). Moreover, denudation rates in the eastern piedmont, where foreland sediments are not incised, are similar within uncertainties to those in the western piedmont, where rivers incise Cenozoic to Quaternary foreland deposits.

We also considered the potential impact of sediments stored in glacial moraines and subsequently mixed with modern fluvial sediments. Most glacial sediments are shielded by ice before being released into the fluvial system and are, therefore, likely to be depleted in cosmogenic nuclides. Here, we assume the most impactful scenario is that glacial sediments have a negligible concentration of cosmogenic nuclides. Fig. 4 provides expected biases on denudation rates for several eroded thicknesses of stored glacial sediments as a function of the proportion of stored glacial materials recycled into river sediments. This calculation shows that denudation rates derived from ^{10}Be in river sediments recycling moraine deposits may overestimate basin-average denudation rates if the denudation rate is very low (i.e. <20 m/Ma; Fig. 4a–c). In most cases, the recycling of a significant proportion (>10–20%) of glacial material is required to bias the denudation rate beyond the analytical uncertainties. For higher denudation (e.g. 135 m/ Ma) the denudation rates can be overestimated only if the recycled moraine is thick (>50 m; Fig. 4d).

Nonetheless, in the eastern Tianshan, most till moraines are thin (~10–20 m, e.g. Li et al., 2014) and the overall volume of potentially recycled glacial sediments is probably too low to significantly bias the signal. For instance, in the Urumqi basin, where 20 m thick moraines were observed (e.g. Li et al., 2014), given the surface of 1.23×10^3 km^2 of the basin and assuming denudation of 18 m/Ma, to reach 20% of recycled sediment, 5.5×10^3 m3 of moraine sediments must be reworked. Assuming simple 40 m-width per 20 m-high triangular shape moraine, would implies a total length of ~14 km of morainic ridge removed each year, which is unrealistic given the moraine remains observed and the associated maximum extension of past glaciers (e.g. Li et al., 2014). In conclusion, our mixing model suggests that our ^{10}Be-derived basin-averaged denudation rates are not overestimated because the incorporation of ^{10}Be-depleted, temporarily stored sediments (fluvial, colluvial, or glacial) is limited in the studied basins.

Alternatively, our calculations suggest that only a low proportion of thin transitory sediments is needed to significantly increase cosmogenic concentrations in sediments transported by rivers, resulting in underestimated basin-averaged denudation rates (Figs. 3, 4).

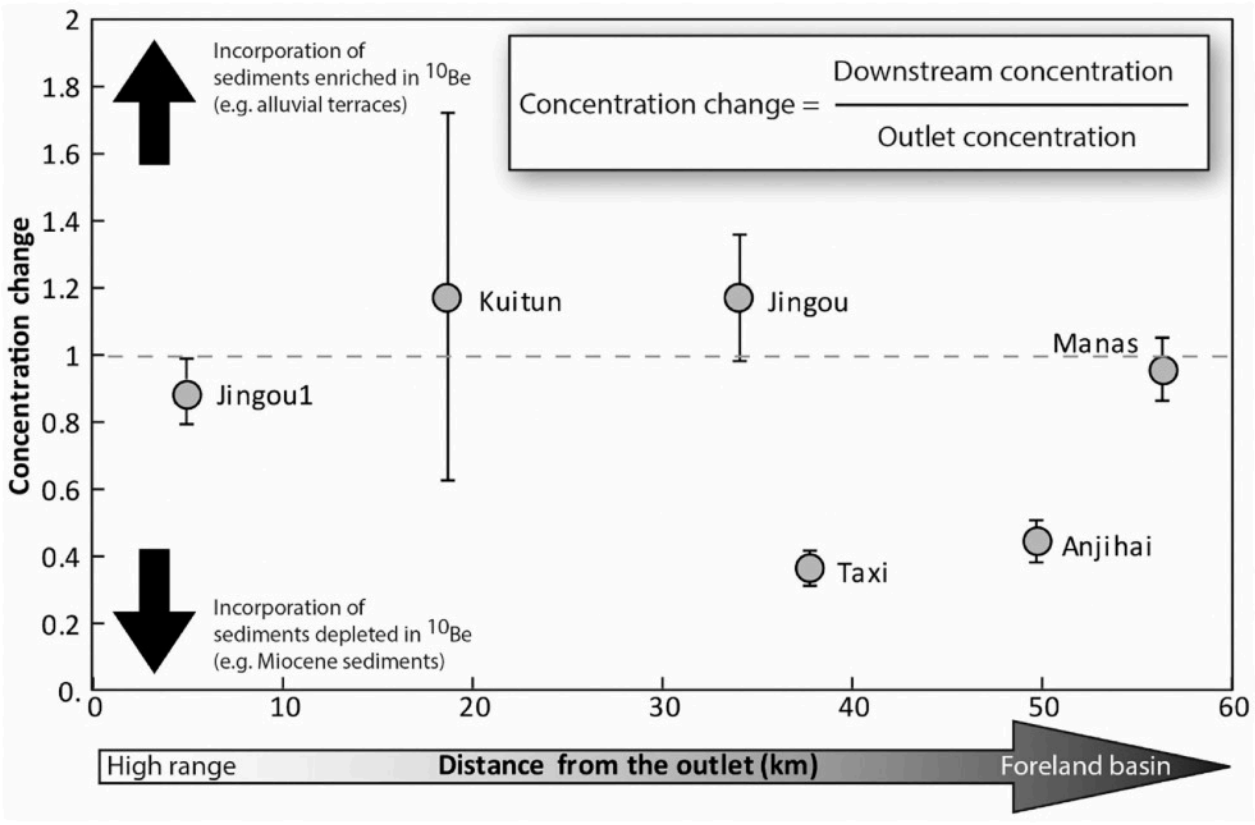

Fig. 5. ^{10}Be concentrations of measured downstream in six rivers draining the northern piedmont (see Fig. 1 for locations) relative to those measured upstream (i.e. at the outlets from the high range) in the same rivers. This ratio represents the relative concentration changes between the outlets from the high range and locations several kilometers downstream within the foreland piedmont.

Indeed, if uneroded and well preserved in the basin, near-surface transitory sediments can be enriched in cosmogenic nuclides. However, none of our samples collected downstream in the piedmont show, within uncertainties, a significant increase of cosmogenic concentrations compared to those collected upstream, despite the rivers deeply incising alluvial terraces up to 100 m thick (Fig. 5). Furthermore, Quaternary fluvial terraces are generally poorly preserved in the southern Tianshan and thus should not bias the cosmogenic signal. In conclusion, the cosmogenic concentrations measured in Tianshan river sediments pro- vide robust estimates of recent denudation rates and can be used to accurately balance the sediment flux across the range.

4.2. Timescale and steadiness of shortening and denudation rates

Geomorphological markers record the mean deformation rate since their abandonment, at 1.3 Ma to 68 ka in this dataset (Charreau et al., 2020; Charreau et al., 2018; Saint-Carlier et al., 2016). Slip rates may vary across structures while summing all mean values from individual structures assumes that all structures were simultaneously active, which may not always be the case. Nevertheless, the geomorphologically deduced total crustal shortening rate of 9.5 ± 3.1 mm/a is remarkably similar to the horizontal velocity documented by GPS data (Fig. 2). This suggests that the total deformation rate is robust and has remained steady across the range since at least 68 ka.

Denudation rates derived from modern river sands are integrated over time scales of ~1–6 ka, whereas deformation rate estimates are integrated over time scales of ~100 ka to 1 Ma in this dataset. This discrepancy may hamper the direct comparison of these rates to establish the balance between denudation and the tectonic crustal flux during the Pleistocene. The Tianshan climate varied throughout the Pleistocene (Prud'homme et al., 2021) and currently differs between the two pied- monts with 2–4 times more rainfall in the northern piedmont (~100–200 mm/a) than in the southern (<50 mm/a). For example, the impact of the last deglaciation is more pronounced in the northern Tianshan, where rivers have more deeply incised the piedmont since 20–10 ka (Malatesta and Avouac, 2018), probably associated with a discreet pulse and release of glacial sediments stored in upstream valleys. One may therefore suspect that spatial and temporal variations of denudation rates and sediment fluxes might prevent the balancing of sediment fluxes derived from recent (<6 ka) denudation rates with Pleistocene crustal fluxes.

Based on in-situ cosmogenic analyses of foreland sediments dated from 0 to 9 Ma, Puchol et al. (2017) showed that denudation rates in the Tianshan have remained relatively steady during the Quaternary, at least in the Kuitun, Jingou He, and Yaha basins. Paleodenudation rates for other drainage catchments can be also derived from in-situ cosmogenic ^{10}Be depth profiles measured across fluvial terraces. Although the main goal of these profiles was to constrain the abandon ages of the studied alluvial surfaces, these datasets also provide the inherited cosmogenic ^{10}Be concentrations of the fluvial sediments at the time of their deposition, which is assumed to be nearly the same as the abandonment age of the surface. Hence, past denudation rates at the time of deposition can be calculated from the inherited ^{10}Be concentrations recorded in each terrace. The paleo-denudation rates can be then calculated assuming the paleo-cosmogenic basin average production rates similar to modern values. Rigorously, this assumes no change in the extent of the

drainage basins which could be a strong hypothesis. However, basin average cosmogenic production rates are mainly function of the elevation and hypsometry of the basins. At the time scale considered here (0–150 ka), even if drainage basin reorganization occurred, the associated changes in elevation and hypsometry and, hence, in cosmogenic production rates, were likely negligible. Compiling all existing depth profiles reported for the eastern Tianshan, we estimated inherited ^{10}Be concentrations and paleo-denudation rates from 11 Pleistocene and Holocene terraces, corresponding to seven ba- sins for which recent denudation rates have been documented.

To account for past changes in glacial coverage, we considered two end-member scenarios. In the first, we assumed that no glaciers were present and computed the basin-averaged ^{10}Be production rates accordingly. This scenario yields maximum estimates of production rates and derived denudation rates. Conversely, in the second scenario, we calculated basin-averaged cosmogenic production rates considering the maximum possible glacial extent during the Last Glacial Maximum (LGM), which we reconstructed using a simple 2D glacier-flow model in Matlab©. This model describes the ice extent at equilibrium with the climate, ice motion is determined under the shallow-ice approximation, and the surface mass-balance is computed from a positive degree-day approach including a positive degree-day mass-balance based on paleo-ELA reconstructions (Blard et al., 2007). Model inputs are (i) the landscape topography, for which we used a 1400-m-resolution DEM, and (ii) the local meteorological conditions at Urumqi. Cooling of 9 $^{\circ}$C under constant precipitation was necessary to reproduce the LGM paleo- ELA reconstructions at ca. 2700 m elevation (e.g. Li et al., 2014). One of the model outputs is glacier thickness, which we converted into shielding factors to estimate subglacial cosmogenic ^{10}Be production rates (Supplementary Fig. A). This approach yields minimum estimates of ^{10}Be production rates and denudation rates.

The maximum and minimum denudation rates estimated by considering the above scenarios are reported in Table 2, alongside ratios comparing paleo- and recent denudation rates in the same basin. Estimated paleo-denudation rates during ~140–5 ka range from 0.12 ± 0.03 to 0.62 ± 0.06 mm/a. The correction for glacial coverage is limited (in average LGM glacier corrected production rates are 8% lower than production rates without glaciers at all); within uncertainties, denudation rates calculated considering glacial cover are similar to those calculated for the absence of glaciers (Fig. 6c). Furthermore, Pleistocene denudation rates are also generally similar, within uncertainties, to recent denudation rates: the average ratios of paleo- to recent denudation rates are 0.9 ± 0.1 and 0.8 ± 0.1 for the glacial coverage and glacier-free scenarios, respectively. These ratios have remained relatively steady since ~140 ka, the age of the oldest dated alluvial terrace (Fig. 6). However, alluvial terrace deposition may result from particular hydrological conditions that favor sediment aggradation over incision. This observed steadiness might therefore reflect sample aliasing, with terrace sediments always recording similar denudation conditions. Nonetheless, the fact that terraces were deposited under various climatic conditions (Fig. 6a) is reassuring, suggesting that the steadiness of the denudation rates is robust and unaffected by significant aliasing.

Combined, these results suggest that both denudation rates and shortening rates have remained steady since the Pleistocene and that the recent ^{10}Be-derived sediment fluxes can be compared to crustal thickening as derived from Pleistocene shortening rates.

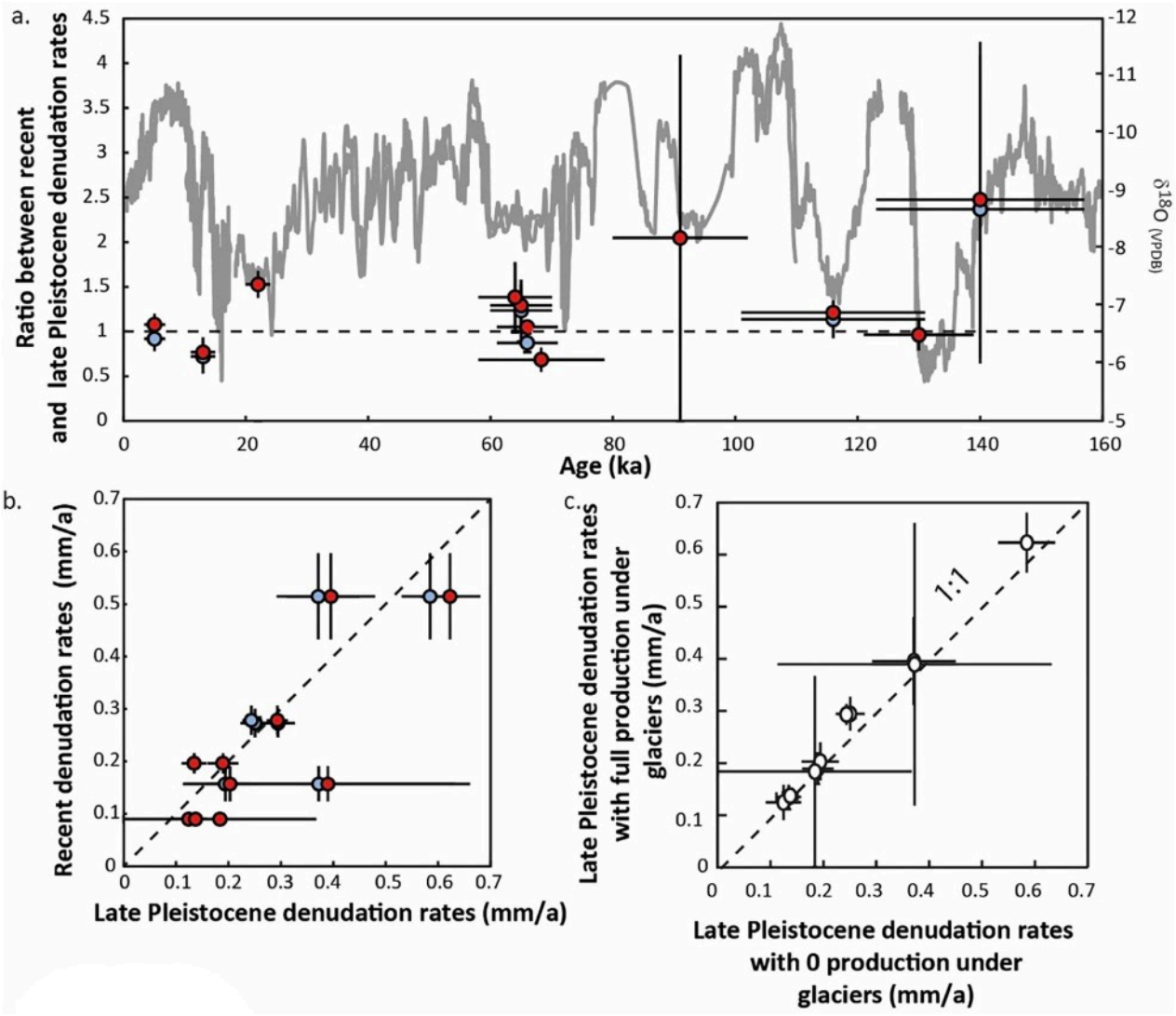

Fig. 6. Comparisons between late Pleistocene and recent denudation rates. (a) late Pleistocene denudation rates normalized to the recent values as a function of the time of abandonment of the dated geomorphological surface. Red and blue circles indicate normalized denudation rates considering maximum and negligible cosmogenic production rates under glaciers within the drainage basin, respectively (see Supplementary Information for details regarding our modeling of maximal glacial extents). The gray curve indicates oxygen isotopic values measured in speleothems in the Hulu and Sanbao caves in China, which document climate variability in Central Asia (Cheng et al., 2016). (b) Recent basin-averaged denudation rates derived from ^{10}Be cosmogenic analyses of modern river sands compared to late Pleistocene denudation rates in the same drainages determined from ^{10}Be cosmogenic depth profile analyses of alluvial terraces (see Table 2 for references). (c) Comparison between late Pleistocene denudation rates calculated with and without glacial cover in the studied drainage basins. (For interpretation of the references to colour in this figure legend, the reader is referred to the web version of this article.)

4.3. Total sediment fluxes exported to the foreland basins

The total surface of the sampled basins is ~37.9 × 10^3 km^2, representing ~80% of the total surface of the two Tianshan piedmonts at the considered longitudes. To better and accurately estimate the total sediment fluxes shed from the piedmonts, we also need to constrain the average denudation rates in and sediment fluxes from the remaining 20%, for which no ^{10}Be data is available (i.e. small interfluves). Topography is a direct expression of the numerous processes interacting to shape the landscape and morphometric parameters can therefore be used to extrapolate denudation. Unfortunately, in the studied basins, we could not identify any particular, straightforward relationship between measured denudation rates and the main morphometric parameters, including mean hill slope, mean local relief, and mean elevation (Fig. 7, Supplementary Table B). Therefore, we cannot apply any reliable morphometric relation to extrapolate denudation rates for the unsampled regions, and we have simply estimated the sediment flux from these regions using the average denudation rates of the surrounding northern and southern Tianshan basins. The total unsampled areas are 6.1 × 10^3 km^2 and 4.7 × 10^3 km^2 in the northern and southern piedmonts, respectively. Assuming respective average denudation rates of 0.20 ± 0.04 mm/a and 0.11 ± 0.02 mm/a in unsampled basins of the northern and southern Tianshan, we obtain additional sediment fluxes from these areas of 12.4 ± 6.0 × 10^5 m^3/a and 5.1 ± 3.0 × 10^5 m^3/a, for total sediment fluxes from the northern and southern piedmonts of 66.6 ± 9.8 × 10^5 m^3/a and 21.5 ± 5.9 × 10^5 m^3/a, respectively.

This discrepancy between the two sides of the range is likely related to the contrasting precipitation across the range. Indeed, the highly elevated topography of the range represents a strong orographic barrier to southward Artic and Central Asian air masses. Consequently, the northern windward side of the range receives much more rain than the strongly arid southern, leeward side. The total combined sediment flux exported from both piedmonts toward the Tarim and Junggar basins is thus between 72.4 × 10^5 m^3/a and 103.8 × 10^5 m^3/a.

4.4. Denudation vs. tectonic shortening

Our results indicate that only 6–15% of the crustal influx due to convergence across the orogen is redistributed through denudation and transported to the Tarim and Junggar basins. This calculation neglects denudation and sediment production in the internal part of the range because we were unable to sample enough drainage basins to provide a robust estimation of denudation rates and sediment fluxes there. However, the few denudation rates we were able to measure are low (<0.2 mm/a; Table 1), suggesting low sediment fluxes. Moreover, most sediments produced in this internal zone are shed toward the Bayanbulak, Turpan, and Yili basins. Bayanbulak is a marsh basin at high and steady elevation, and a large lake has developed in the middle of the Turpan basin. Therefore, these two basins likely trap and store most incoming sediments (Figs. 1, 2). Only sediments exported westward to the Yili basin may exit the system considered in our mass balance; however, given the surface area of and calculated denudation rates for this basin (see Fig. 1, Table 1), the sediment flux is likely too low to compensate for the imbalance between denudation and crustal thickening.

Due to the clockwise rotation of the Tarim crust, deformation across the Tianshan decreases eastward. Consequently, assuming a constant shortening rate of 9.6 mm/a along a 270-km-long section may overestimate the total crustal flux.

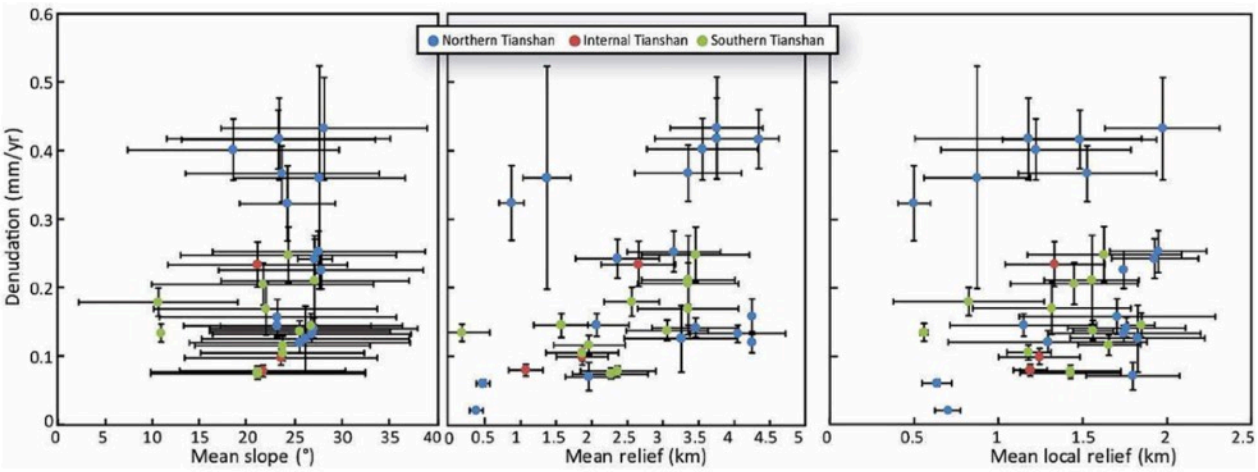

Fig. 7. Recent basin-averaged denudation rates in each studied basin compared to, from left to right, mean slope, mean relief, and mean local relief. The mean relief is the maximum elevation minus the minimum elevation fo the basin. The local relief was calculated over square 5 × 5 km areas. The errors bars represent the standard deviation of the slope, the elevation and the mean local relief.

The eastward decrease of shortening accommodated across the range varies from 4.9 to 10.8 km per degree of longitude (Avouac et al., 1993). Assuming that the onset of deformation across the range was between 25 and 10 Ma (e.g. Charreau et al., 2009; Hendrix et al., 1994), the corresponding eastward decrease in deformation rates is from 0.2 to 1.1 mm/a per degree of longitude. This bias is likely already encompassed within the shortening uncertainties and is also insufficient to compensate for the flux imbalance.

In our mass balance calculation, we considered that the entirety of the Jungar and Tarim crusts are accreted to the Tianshan range, which is likely a simplification. In many mountain ranges, only a proportion of the subducting crust contributes to the orogeny, for example via underplating, whereas the remaining crust is subducted toward the mantle (e.g. Simoes et al., 2007). However, in the case of pure equilibrium and at a shortening rate of 9.6 mm/a across the 270-km-long section, our estimated denuded volume represents only 5 km of accreted crust. This thickness is consistent with the deepest decollement observed in the piedmonts (e.g. Hubert-Ferrari et al., 2007) but requires that: (1) the remaining 37 and 30 km of crustal thickness are subducted and do not contribute to the orogeny, and (2) deformation and crustal thickening are restricted to the piedmonts while 15 to 45% of the total shortening across the range is accommodated by inner structures (Charreau et al., 2017). This second scenario is unrealistic, suggesting that, even if our mass balance overestimates the disequilibrium between the accretionary and denudational fluxes because part of the crust is subducting, the disequilibrium itself is robust.

In numerical models of uniform crustal materials, when the accretionary flux exceeds the denudational flux, ranges first grow by uplifting the topography (Beaumont et al., 2004; Vanderhaeghe, 2012). In the eastern Tianshan, given a mean denudation rate of 0.1 mm/a, a crustal

thickening of 1.3 mm/a, the net change in crustal thickness (ΔT) is 1.2 mm/a. Assuming a compensation by local isostasy over a broad scale, the average surface uplift rate is equal to: $\Delta H = A.\ \Delta T$ with $A = (\varrho_m - \varrho_c)/\ \varrho_m$ (see Molnar and Lyon-Caen (1988) for a demonstration of this equation) where ϱ_m(~3.1) and ϱ_c (~2.7) are the density of the mantle and the crust, respectively. The average surface uplift rate is therefore ~0.2 mm/a. In the case of a non-local isostasy, for instance with flexural compensation, $A > (\varrho_m - \varrho_c)/\ \varrho_m$ (see Turcotte and Schubert (2002)) and hence the surface uplift rate > 0.2 mm/a.

Numerical models also predict that orogens may grow by increasing their width (Willett et al., 2001). In particular, thermomechanical models coupled with surface processes underscore the critical role of denudation in maintaining orogen topography (Avouac and Burov, 1996) and controlling orogen width and the distribution of deformation across the orogen (Willett et al., 2001). For instance, Rosenberg et al. (2015) suggested that the Alps widen at increased rates when denudation rates decrease. In the Tianshan, morphotectonic analyses and fold modeling of growth strata suggest that deformation across the external fold and thrust belts of the foreland piedmonts likely accelerated during the Quaternary (Charreau et al., 2020; Charreau et al., 2018; Hubert-Ferrari et al., 2007; Saint-Carlier et al., 2016). Fold modeling and magnetostratigraphic dating of growth strata also show that most folds in both piedmonts were initiated in sequence, with the youngest structures localized in the external parts of the piedmonts (Charreau et al., 2020; Charreau et al., 2008; Da¨eron et al., 2007; Gao et al., 2020). Seismic profiling in the Tarim and Junggar basins also reveals the existence of new blind structures localized at the front of the Dushanzi-Anjihai-Tugulu fold-and-thrust belt (Qiu et al., 2021) and Yakeng anticline (Hubert-Ferrari et al., 2005), which are the most frontal of the emerged structures in the northern and southern Tianshan, respectively. Altogether, this evidence suggests that deformation across the Tianshan has recently propagated toward the border of the range (Charreau et al., 2018). The width of the Tianshan range thus increases to compensate for the elevating topography due to the flux imbalance.

Another clue that the Tianshan has attained neither its maximum elevation nor maximum width comes by comparing its geometry to other convergent mountain ranges around the world (Fig. 8). Globally, convergent ranges define a general trend from low (<3 km elevation) and narrow (<250 km wide) triangular orogenic wedges (e.g. French and New Zealand Alps, Pyrenees) to wide (>300 km wide) orogenic plateaus at broadly similar higher elevations (5–7 km) (Vanderhaeghe, 2012) (Fig. 8). This topographic trend may suggest that triangular orogenic wedges will increase their width and elevation until a thermomechanical stability is reached. Based on its elevation and width, the Tianshan plots between narrow, low orogenic wedges and large orogenic plateaus (Fig. 8), reinforcing the notion that it has not yet attained its maximum elevation or width. However, several low- elevation (<3 km) but wide (>400 km) ranges (Zagros, Rocky Mountains, Caucasus, Sierra Madre) plot off the general trend. These particular convergent zones share structural and geological complexities inherited from histories of previous terrane accretion, which may result in rheological weaknesses and heterogeneities that favor distributed deformation and the rise of large-scale topography during the final phase of collision/convergence. Indeed, numerical thermomechanical modeling suggests that inheritance facilitates the propagation of basement deformation and increases orogen width (Erdo˝s et al., 2014). In the Tianshan, numerous structures are inherited from

its long Paleo-Mesozoic geological history. During the early Cenozoic, thermochronological studies suggest that the deformation associated with the India-Asia collision was first focused on the reactivation of these pre-existing structures (Jolivet et al., 2010). Several studies have also demonstrated that the pre-Cenozoic topography comprised individual ranges separated by basins (Morin et al., 2019). The irregular and complex topography of the Tianshan is therefore likely due to a combination of orogenic widening due to low denudation rates and promoted by preexisting structures and the reactivation of basins and relief as deformation propagates outward.

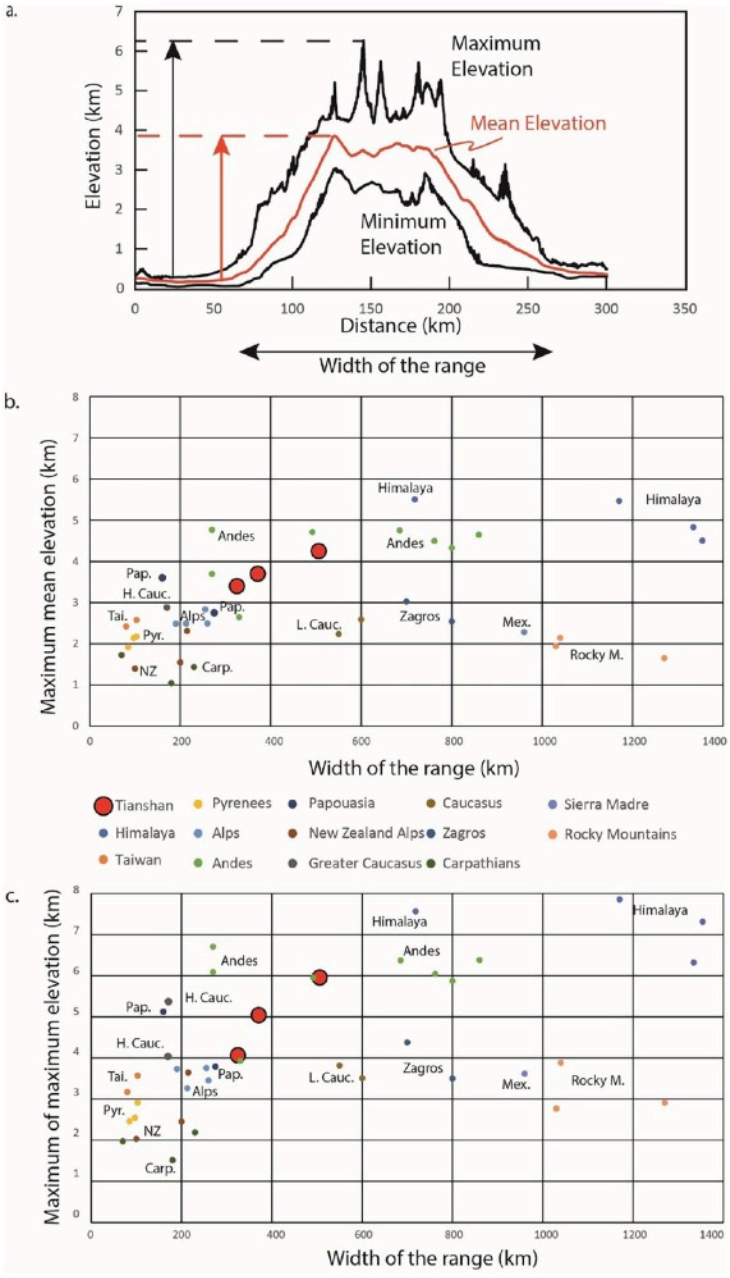

Fig. 8. (a) Example swath topographic profile demonstrating how the width, maximum mean elevation, and maximum of maximum elevation of each range is measured. To estimate the width, the limits between the basin and the orogen were defined as the point where the relief (difference between minimum and maximum elevation) and the slope of the topography decrease rapidly. The maximum mean elevation is the difference between the elevation of the surrounding basin and the maximum of the mean elevation observed within the range. The maximum of maximum elevation is the difference between the elevation of the surrounding basin

and the maximum of the maximum elevation observed within the range. (b, c) Range width compared to maximum mean elevation and the maximum of the maximum elevation, respectively.

That said, other important questions are whether these mechanisms of topographic building including fluxes disequilibrium, widening of the range and reactivation of pre-existing structures, are either recent or were sustained other longer-time and, if the second, since when? And what is the respective role of each process (disequilibrium, widening and reactivation)? Mio-Pliocene sediment progradation rates measured across the two piedmonts were ~ 6 mm/a (Charreau et al., 2009). If we assume sediment progradation rates to be mainly controlled by the propagation of the deformation toward the piedmonts, this value may represent crude estimate of the long-term deformation rates across the entire range. No detailed (time scale <1 Ma) long-term quantifications of outward sediments fluxes are available. However, paleo-denudation rates were reconstructed across 4 drainage basins in the Eastern Tianshan (Charreau et al., 2011; Puchol et al., 2017). The four records display similar trends of continuously increasing denudation between ca. 9 Ma and the present, with relatively high but steady rates since 4 Ma (Puchol et al., 2017). Together, these results may suggest that the disequilibrium in fluxes exist at least since Miocene when the range rejuvenated ~11 Ma ago (Bullen et al., 2001). Growth strata revealed by seismic analysis and/or fold modeling and thermochronological analysis across different folds into the forelands suggest that deformation also initiated during Miocene (Charreau et al., 2018; Charreau et al., 2018; Däeron et al., 2007; Hendrix et al., 1994; Hubert-Ferrari et al., 2007; Saint-Carlier et al., 2016; Sun et al., 2009b). This likely suggests that the widening of the range already worked at that time as well.

5. Conclusions

Our study provides an important new dataset of recent (0–6 ka) and Pleistocene (<140 ka) denudation rates in Central Asia, which we used to estimate sediment outflux across the Eastern part of the Tianshan range. We also quantified the total Pleistocene shortening accommodated across this range to derive the crustal influx. Our detailed, quantitative results document a flux imbalance across this large intracontinental orogen. These data improve our understanding of the growth of one of the most active orogenic belts in the world, which is thought to have impacted the global climate. Our study suggests that the Tianshan is in an unsteady state with a strong flux imbalance. To compensate for this disequilibrium, the range grows laterally and likely reactivates inherited structures, yielding complex and irregular topography comprising individual ranges separating intramountain basins. This pattern may have existed at least since the Miocene. However, more detailed quantification of both longer-term Miocene deformation rates and longer-term sediment fluxes are still needed to better understand the long-term building history of the Tianshan. Similarly, the timing and duration of the reactivation of inherited structures within the internal part of the range and the amount of deformation they have accommodated are unknown. These data would be critical to better understand the role of inheritance during mountain building. Future numerical modeling may also elucidate the respective roles of inherited structures and low denudation rates in determining the width and complexity of the Tianshan topography.

Authors statement

Julien Charreau conceptualization, funding acquisition, investiga- tion, data curation, writing, review and editing.

Pierre-Henri Blard - field sampling, sample treatments, cosmogenic analysis, writing and editing.

Jérôme Lavé - field sampling, writing and editing.
Stéphane Dominguez – field sampling, writing and editing.
Wang Sheng li – Field work organization, field sampling, writing

and editing.

Declaration of Competing Interest

We do not declare any conflict of interest and certify that all funding and associated organizations have been declared in the acknowledgements.

Data availability

All data are presented in the table in the article.

Acknoledgements

This study was financed French INSU Syster program. We thank three anonymous reviewers for their careful reviews which greatly improved the overall quality of our manuscript. This is CRPG contribution n2839.

Appendix A. Supplementary data

Supplementary data to this article can be found online at https://doi. org/10.1016/j.tecto. 2022.229702.

References

Antonelli, A., Nylander, J.A.A., Persson, C., Sanmartı, I., 2009. Tracing the impact of the Andean uplift on Neotropical plant evolution. Proc. Natl. Acad. Sci. 106, 9749–9754.

Avouac, J., Burov, E.B., 1996. Erosion as a driving mechanism of intracontinental moutain growth. J. Geophys. Res. 101, 17747–17769.

Avouac, J.P., Tapponnier, P., Bai, M., You, H., Wang, G., 1993. Active Thrusting and Folding along the Northern Tien-Shan and late cenozoic rotation of the Tarim relative to Dzungaria and Kazakhstan. J. Geophys. Res. Earth 98, 6755–6804. https://doi.org/10.1029/92jb01963.

Beaumont, C., Kool, H., Willett, S.D., 1999. Coupled tectonic-surface process models with applications to rifted margins and collisional orogens. In: Summerfield, M. (Ed.), Geomorphology and Globale Tectonics. John Wiley Sons Ltd, New York, pp. 29–55.

Beaumont, C., Jamieson, R.A., Nguyen, M.H., Medvedev, S., 2004. Crustal channel flows: 1. Numerical models with applications to the tectonics of the Himalayan-Tibetan orogen. J. Geophys. Res. B Solid Earth 109, 1–29. https://doi.org/10.1029/ 2003JB002809.

Blard, P.-H., Lave, J., Pik, R., Wagnon, P., Bourles, D., 2007. Persistence of full glacial conditions in the Central Pacific until 15,000 years ago. Nature 449, 591–594. Botsyun, S., Sepulchre, P., Donnadieu, Y., Risi, C., Licht, A., Rugenstein, J.K.C., 2019. Revised paleoaltimetry data sho low Tibetan Plateau elevation during the Eocene. Sciences (New York) 946, 1–9. https://doi.org/10.1126/science.aaq1436.

Braun, J., 2006. Recent advances and current problems in modeling processes and their interaction with crustal deformation. In: Buiter, S.J.H., Schreurs, G. (Eds.), Analogue and Numerical Modeling of Crustal-Scale Processes. Geological Society, London, Special Publications, pp. 307–325.

Brown, E.T., Edmond, J.M., Raisbeck, G.M., Yiou, F., Kurz, M.D., Brook, E.J., 1991. Examination of surface exposure ages of Antarctic moraines using in situ produced 10Be and 26Al. Geochim. Cosmochim. Acta 55, 2269–2283.

Bullen, M.E., Burbank, D.W., Garver, J.I., Abdrakhmatov, K.Y., 2001. Late Cenozoic tectonic evolution of the northwestern Tien Shan: new age estimates for the initiation of mountain building. Bull. Geol. Soc. Am. 113, 1544–1559.

Burbank, D.W., 2002. Rates of erosion and their implications for exhumation. Mineral. Mag. 66, 25–52. https://doi.org/10.1180/0026461026610014.

Bureau of the Geological and the Mineral Resources of the Xinjiang Uygur Autonomous Region, 1985. Geological Map of the Xinjiang Uygur Autonomous Region, China. China Geol. Print. House.

Charreau, J., Gilder, S., Chen, Y., Dominguez, S., Avouac, J.-P., Sen, S., Jolivet, M., Li, Y., Wang, W., 2006. Magnetostratigraphy of the Yaha section, Tarim Basin (China): 11 Ma acceleration in erosion and uplift of the Tian Shan mountains. Geology 34, 181. https://doi.org/10.1130/G22106.1.

Charreau, J., Avouac, J.-P., Chen, Y., Dominguez, S., Gilder, S., 2008. Miocene to present kinematics of fault-bend folding across the Huerguosi anticline, northern Tianshan (China), derived from structural, seismic, and magnetostratigraphic data. Geology 36, 871–874. https://doi.org/10.1130/G25073A.1.

Charreau, J., Chen, Y., Gilder, S., Barrier, L., Dominguez, S., Augier, R., Sen, S., Avouac, J.-P., Gallaud, A., Graveleau, F., Wang, Q., 2009. Neogene uplift of the Tian Shan Mountains observed in the magnetic record of the Jingou River section (Northwest China). Tectonics 28, n/a–n/a. https://doi.org/10.1029/2007TC002137.

Charreau, J., Blard, P.H., Puchol, N., Avouac, J.P., Lallier-Verg`es, E., Bourl`es, D., Braucher, R., Gallaud, A., Finkel, R., Jolivet, M., Chen, Y., Roy, P., 2011. Paleo- erosion rates in Central Asia since 9Ma: a transient increase at the onset of Quaternary glaciations? Earth Planet. Sci. Lett. 304, 85–92. https://doi.org/ 10.1016/j.epsl.2011.01.018.

Charreau, J., Saint-Carlier, D., Dominguez, S., Lav´e, J., Blard, P.-H., Avouac, J.-P., Jolivet, M., Chen, Y., ShengLi, W., Borwn, N.D., Malatesta, L.C., Rhodes, E.,
Team, A., 2017. Denudation outpaced by crustal thickening in the eastern Tianshan. Earth Planet. Sci. Lett. 479, 179–191.

Charreau, J., Saint-Carlier, D., Lav´e, J., Dominguez, S., Blard, P.-H., Avouac, J.-P., Brown, N.D., Malatesta, L.C., Wang, S., Rhodes, E.J., 2018. Late Pleistocene acceleration of deformation across the northern Tianshan piedmont (China) evidenced from the morpho-tectonic evolution of the Dushanzi anticline. Tectonophysics 730. https://doi.org/10.1016/j.tecto.2018.02.016.

Charreau, J., Blard, P.-H., Zumaque, J., Martin, L.C.P., Delobel, T., Szafran, L., 2019. Basinga: a cell-by-cell GIS toolbox for computing basin average scaling factors, cosmogenic production rates and denudation rates. Earth Surf. Process. Landf. 44, 2349–2365.

Charreau, J., Sart´egou, A., Saint-Carlier, D., Lav´e, J., Blard, P.-H., Dominguez, S., Wang, S.L., Rao, G., Aster, T., 2020. Late miocene to quaternary slip history across the qiulitag anticline in the southern Tianshan piedmont. Terra Nova 32, 89–96.

Cheng, H., Spo¨tl, C., Breitenbach, S.F.M., Sinha, A., Wassenburg, J.A., Jochum, K.P., Scholz, D., Li, X., Yi, L., Peng, Y., Lv, Y., Zhang, P., Votintseva, A., Loginov, V., Ning, Y., Kathayat, G., Edwards, R.L., 2016. Climate variations of Central Asia on orbital to millennial timescales. Sci. Rep. 5, 1–11. https://doi.org/ 10.1038/ srep36975.

Codilean, A.T., 2006. Calculation of the cosmogenic nuclide production topographic shielding scaling factor for large areas using DEMs. Earth Surf. Process. Landf. 31, 785–794.

Curry, M.E., van der Beek, P., Huismans, R.S., Wolf, S.G., Mun˜oz, J.-A., 2019. Evolving paleotopography and lithospheric flexure of the Pyrenean Orogen from 3D flexural modeling and basin analysis. Earth Planet. Sci. Lett. 515, 26–37. https://doi.org/ 10.1016/j.epsl.2019.03.009.

Däeron, M., Avouac, J.-P., Charreau, J., 2007. Modeling the shortening history of a fault tip fold using structural and geomorphic records of deformation. J. Geophys. Res. 112, B03S13. https://doi.org/ 10.1029/2006JB004460.

Dahlen, F.A., Suppe, J., 1988. In: Clark, S.P., Burchfiel, B.C., Suppe, J. (Eds.), Mechanics, growth, and erosion of mountain belts. Processes in Continental Lithospheric Deformation, Geological Society of America Special Paper, pp. 161–178.

Delunel, R., van der Beek, P.A., Carcaillet, J., Bourl`es, D.L., Valla, P.G., 2010. Frost- cracking control on catchment denudation rates: Insights from in situ produced 10Be concentrations in stream sediments (Ecrins–Pelvoux massif, French Western Alps). Earth Planet. Sci. Lett. 293, 72–83. https://doi.org/10.1016/j.epsl.2010.02.020.

Erdo˝s, Z., Huismans, R.S., van der Beek, P., Thieulot, C., 2014. First-order cotrol of syntectonic sedimentation on crustal-scale structure of mountain belts. J. Geophys. Res. Solid Earth 119, 9042–9061. https://doi.org/10.1002/2014jb011408.

Ferrier, K.L., Kirchner, J.W., Finkel, R.C., 2005. Erosion rates over millennial and decadal timescales at Caspar Creek and Redwood Creek, Northern California Coast Ranges. Earth Surf. Process. Landf. 30, 1025–1038. https://doi.org/10.1002/esp.1260.

Gao, L., Rao, G., Tang, P., Qiu, J., Peng, Z., Pei, Y., Yu, Y., Zhao, B., Wang, R., 2020. Structural development at the leading edge of the salt-bearing Kuqa fold-and-thrust belt, southern Tian Shan, NW China. J. Struct. Geol. 140, 104184 https://doi.org/ 10.1016/j.jsg.2020.104184.

Guan, X., Ma, Y., Lu, H., Jiang, Y., Pang, L., Zheng, X., Li, Y., 2022. Topographic and climatic controls on decadal-scale catchment-basin erosion rates in the northern Chinese Tian Shan. Catena 210, 105862. https://doi.org/10.1016/j. catena.2021.105862.

Guerit, L., Barrier, L., Jolivet, M., Fu, B., M´etivier, F., 2016. Denudation intensity and control in the Chinese Tian Shan: new constraints from mass balance on catchment- alluvial fan systems. Earth Surf. Process. Landf. 41, 1088–1106. https://doi.org/ 10.1002/esp.3890.

Hendrix, M.S., Dumitru, T.A., Graham, A.S., 1994. Late Oligocene-early Miocene unroofing in the Chinese Tian Shan : an early effect of the India-Asia collision. Geology 22, 487–490.

Huang, B., Piper, J.D.A., Peng, S., Liu, T., Li, Z., Wang, Q., Zhu, R., 2006. Magnetostratigraphic study of the Kuche Depression, Tarim Basin, and Cenozoic uplift of the Tian Shan Range, Western China. Earth Planet. Sci. Lett. 251, 346–364.

Hubert-Ferrari, A., Suppe, J., Wang, X., Jia, C., 2005. The Yakeng detachment fold, China. In: Connors, C., Suppe, J. (Eds.), Shaw, J.H. Seismic Interpretation of Contractional Fault-Related Folds, American Association of Petroleum Geologists, pp. 110–113.

Hubert-Ferrari, A., Suppe, J., Gonzalez-Mieres, R., Wang, X., 2007. Mechanism of active folding of the landscape (southern Tianshan, China). J. Geophys. Res. 112 https:// doi.org/10.1029/2006JB004362.

Hurtrez, J.-E., Lucazeau, F., Lav´e, J., Avouac, J.-P., 1999. Investigation of the relationships between basin morphology, tectonic uplift, and denudation from the study of an active fold belt in the Siwalik Hills, Central Nepal. J. Geophys. Res. 104, 12779. https://doi.org/10.1029/1998JB900098.

Jolivet, M., Dominguez, S., Charreau, J., Chen, Y., Li, Y., Wang, Q., 2010. Mesozoic and Cenozoic tectonic history of the central Chinese Tian Shan: reactivated tectonic structures and active deformation. Tectonics 29, 1–30. https://doi.org/10.1029/ 2010TC002712.

Jolivet, M., Barrier, L., Dominguez, S., Guerit, L., Heilbronn, G., Fu, B., 2014. Unbalanced sediment budgets in the catchment-alluvial fan system of the Kuitun River (northern Tian Shan, China): implications

for mass-balance estimates, denudation and sedimentation rates in orogenic systems. Geomorphology 214, 168–182. https://doi. org/10.1016/j.geomorph.2014.01.024.

Li, Yingkui, Liu, G., Chen, Y., Li, Yanan, Harbor, J., Stroeven, A.P., Caffee, M., Zhang, M., Li, C., Cui, Z., 2014. Timing and extent of Quaternary glaciations in the Tianger Range, eastern Tian Shan, China, investigated using 10 Be surface exposure dating. Quat. Sci. Rev. 98, 7–23. https://doi.org/10.1016/j.quascirev.2014.05.009.

Liu, Y., M´etivier, F., Gaillardet, J., Ye, B., Meunier, P., Narteau, C., Lajeunesse, E., Han, T., Malverti, L., 1Institut, 2011. Erosion rates deduced from seasonal mass balance along the upper Urumqi River in Tianshan. Solid Earth 283–301. https:// doi.org/10.5194/se-2-283-2011.

Malatesta, L.C., Avouac, J.P., 2018. Contrasting river incision in north and South Tian Shan piedmonts due to variable glacial imprint in mountain valleys. Geology 46, 659–662. https://doi.org/10.1130/G40320.1.

Martin, L.C.P., Blard, P.H., Balco, G., Lav´e, J., Delunel, R., Lifton, N., Laurent, V., 2017. The CREp program and the ICE-D production rate calibration database : a fully parameterizable and updated online tool to compute cosmic- ray exposure ages. Quat. Geochronol. 38, 25–49. https://doi.org/10.1016/j.quageo.2016.11.006. M´etivier, F., Gaudemer, Y., 1997. Mass transfer between eastern Tien Shan and adjacent basins (Central Asia): constraints on regional tectonics. Geophys. J. Int. 128, 1–17.

Molnar, P., England, P., 1990. Late Cenozoic uplift of mountain ranges and global climate change - Chicken or egg ? Nature 346, 29–34.

Molnar, P., Lyon-Caen, H., 1988. Some simple physical aspects of the support, structure, and evolution of mountain belts. Spec. Pap. Geol. Soc. Am. 218, 179–207. https:// doi.org/10.1130/SPE218-p179.

Molnar, P., Tapponnier, P., 1975. Cenozoic tectonics of Asia : Effects of a Continental Collision. Science 189 (80), 419–426.

Morin, J., Jolivet, M., Barrier, L., Laborde, A., Li, H., Dauteuil, O., 2019. Planation surfaces of the Tian Shan Range (Central Asia): Insight on several 100 million years of topographic evolution. J. Asian Earth Sci. 177, 52–65. https://doi.org/10.1016/j. jseaes.2019.03.011.

Nishiizumi, K., Imamura, M., Caffee, M.W., Southon, J.R., Finkel, R.C., McAninch, J., 2007. Absolute calibration of 10Be AMS standards. Nucl. Instrument. Meth. Phys. Res. Sect. B-Beam Interact. Mater. Atoms 258, 403–413.

Prud'homme, C., Scardia, G., Vonhof, H., Guinoiseau, D., Nigmatova, S., Fiebig, J., Gerdes, A., Janssen, R., Fitzsimmons, K.E., 2021. Central Asian modulation of Northern Hemisphere moisture transfer over the late Cenozoic. Commun. Earth Environ. 2, 1–8. https://doi.org/10.1038/s43247-021-00173-z.

Puchol, N., Charreau, J., Blard, P., Lav´e, J., Dominguez, S., Pik, R., Saint-carlier, D., ASTER Team, 2017. Limited impact of Quaternary glaciations on denudation rates in Central Asia. Geol. Soc. Am. Bull. 129, 479–499.

Qiu, J., Rao, G., Yu, Y., Wang, X., Peng, Z., Gao, L., Yang, D., Xiao, L., Yao, Q., 2021. Control of multiple detachments on structural development in the southern Junggar Fold-and-Thrust Belt, Northern Tian Shan: implications for seismic hazard assessment. Tectonics 40, 1–25. https://doi.org/10.1029/2021tc006712.

Raup, B., Racoviteanu, A., Khalsa, S.J.S., Helm, C., Armstrong, R., Arnaud, Y., 2007. The GLIMS geospatial glacier database: a new tool for studying glacier change. Glob. Planet. Chang. 56, 101–110.

Rosenberg, C.L., Berger, A., Bellahsen, N., Bousquet, R., 2015. Relating orogen width to shortening, erosion, and exhumation during Alpine collision. Tectonics 34, 1306–1328. https://doi.org/10.1002/2014TC003736.

Saint-Carlier, D., Charreau, J., Lav´e, J., Blard, P.-H., Dominguez, S., Avouac, J.P., Wang, S., Arnold, M., Aumaître, G., Keddadouche, K., L´eanni, L., Chauvet, F., Bourl´es, D.L., 2016. Major temporal variations in shortening rate absorbed along a large active fold of the southeastern Tianshan piedmont (China). Earth Planet. Sci. Lett. 434, 333–348. https://doi.org/10.1016/j.epsl.2015.11.041.

Simoes, M., Avouac, J.P., Beyssac, O., Goffe, B., Farley, K.A., Chen, Y.-G., 2007. Mountain building in Taiwan: a thermokinematic model. J. Geophys. Res. B Solid Earth 112, 1–25. https://doi.org/10.1029/12006JB004824.

Stone, J.O., 2000. Air pressure and cosmogenic isotope production. J. Geophys. Res. Solid Earth 105, 23753–23759.

Su, P., He, H., Wei, Z., Lu, R., Shi, F., Sun, H., Tan, X., Hao, H., 2018. A new shortening rate across the Dushanzi anticline in the northern Tian Shan Mountains, China from lidar data and a seismic reflection profile. J. Asian Earth Sci. 163, 131–141. https:// doi.org/10.1016/j.jseaes.2018.06.008.

Sun, J., Li, Y., Zhang, Z., Fu, B., 2009a. Magnetostratigraphic data on Neogene growth folding in the foreland basin of the southern Tianshan Mountains. Geology 37, 1051–1054. https://doi.org/10.1130/G30278A.1.

Sun, Jimin, Li, Y., Zhang, Z., Fu, B., 2009b. Magnetostratigraphic data on Neogene growth folding in the foreland basin of the southern Tianshan Mountains. Geology. https://doi.org/10.1130/G30278A.1.

Thompson, S.C., Weldon, R.J., Rubin, C.M., Abdrakhmatov, K., Molnar, P., Berger, G.W., 2002. Late Quaternary slip rates across the central Tien Shan. Kyrgyzstan, Central Asia 107. https://doi.org/10.1029/2001JB000596.

Turcotte, D., Schubert, G., 2002. Geodynamics.

Uppala, S.M., KÅllberg, P.W., Simmons, A.J., Andrae, U., Bechtold, V.D.C., Fiorino, M., Gibson, J.K., Haseler, J., Hernandez, A., Kelly, G.A., Li, X., Onogi, K., Saarinen, S., Sokka, N., Allan, R.P., Andersson, E., Arpe, K., Balmaseda, M.A., Beljaars, A.C.M., Van De Berg, L., Bidlot, J., Bormann, N., Caires, S., Chevallier, F., Dethof, A., Dragosavac, M., Fisher, M., Fuentes, M., Hagemann, S., Ho´lm, E., Hoskins, B.J., Isaksen, L., Janssen, P.A.E.M., Jenne, R., Mcnally, A.P., Mahfouf, J.-F., Morcrette, J.- J., Rayner, N.A., Saunders, R.W., Simon, P., Sterl, A., Trenberth, K.E., Untch, A., Vasiljevic, D., Viterbo, P., Woollen, J., 2005. The ERA-40 re-analysis. Q. J. R. Meteorol. Soc. 131, 2961–3012. https://doi.org/10.1256/qj.04.176.

Vanderhaeghe, O., 2012. The thermal-mechanical evolution of crustal orogenic belts at convergent plate boundaries: a reappraisal of the orogenic cycle. J. Geodyn. 56–57, 124–145. https://doi.org/10.1016/j.jog.2011.10.004.

Whipp, D.M., Beaumont, C., Braun, J., 2014. Feeding the “aneurysm”: Orogen-parallel mass transport into Nanga Parbat and the western Himalayan syntaxis. J. Geophys. Res. Solid Earth 119, 5077–5096. https://doi.org/10.1002/2013JB010929.

Willett, S.D., Brandon, M.T., 2002. On steady state in mountain belts. Geology 30, 175–178.

Willett, S.D., Slingerland, R., Hovius, N., 2001. Uplift, shortenning, and steady state topography in active mountain belts. Am. J. Sci. 301, 455–485.

Yang, S., Jie, L.I., Qi, W., 2008. The Deformation Pattern and Fault Rate in the Tianshan Mountains Inferred from GPS Observations, p. 51. https://doi.org/10.1007/s11430- 008-0090-8.